Subspace identification for operational modal analysis

Edwin Reynders and Guido De Roeck

Katholieke Universiteit Leuven, Structural Mechanics Division
Kasteelpark Arenberg 40, B-3001 Leuven

Abstract This chapter deals with the estimation of modal parameters from measured vibration data using subspace techniques. An in-depth review of subspace identification for operational modal analysis is provided. In addition, two recent developments are emphasised: the estimation of the probability density function of the modal parameters, and the use of an exogenous force in addition to the unmeasured operational excitation.

1 Introduction

Vibration-based SHM methods very often rely on modal parameters that are estimated from measured vibration data. Classical *Experimental Modal Analysis* (EMA) techniques obtain the modal parameters from input-output measurements, i.e., measured, artificial forces are applied to the structure, and the response to these forces is recorded. The response to unmeasured, ambient forces is considered as unwanted *noise*. In general, such EMA methods are not suitable for large structures and buildings because these structures are inherently tested in operational rather than in laboratory conditions, and the contribution of the measured forces to the total structural response is usually rather low. A bridge for instance can only be excited to a limited vibration level by an artificial excitation source such as a shaker, unless it has a very heavy mass. This implies that the ever-present ambient excitation, due to for example wind or traffic, can most often not be neglected, especially at low frequencies. Output-only or *Operational Modal Analysis* (OMA) techniques have therefore been developed. They extract the modal parameters from the dynamic response to operational forces. The unmeasured, ambient forces are usually modeled as stochastic quantities with unknown parameters but with known behavior, for example, as white noise time-series with zero-mean and unknown covariances. Peeters and De Roeck (2001) provide a review of operational modal analysis techniques.

A. Deraemaeker et al.(eds.), *New Trends in Vibration Based Structural Health Monitoring*

However, the OMA approach has two disadvantages when compared to EMA: the mode shapes can not be mass-normalised, and the frequency content of the excitation is usually narrow-banded. For these reasons, there has been an increasing interest in the last few years towards combined modal testing techniques, also called hybrid vibration testing or *Operational Modal Analysis with eXogenous inputs* (OMAX), where an artificial force is used in operational conditions. The main difference between OMAX and the traditional EMA approach is that the operational forces are included in the identified system model: they are not considered as noise, but as useful excitation. As a consequence, the amplitude of the artificial forces can be equal to, or even lower than the amplitude of the operational forces. This is of crucial importance for the modal testing of large structures. It allows the use of excitation devices that are small and practical when compared to the actuators that are needed for EMA testing such as electromechanical or hydraulic shakers, which are heavy and difficult to transport.

This chapter deals with the estimation of modal parameters from measured vibration data using time-domain subspace identification methods, both from the OMA and the OMAX perspective. These methods identify a discrete-time state-space model. In Section 2, it is demonstrated that this is a valid model for a vibrating structure, by deriving it from a finite element description. The deterministic state-space model is then extended with unobserved inputs and output disturbances, which are both modeled as stochastic quantities. Section 3 provides insight into the basic ideas that lie behind subspace methods; the subspace identification algorithms themselves are presented in Section 4. Two important recent developments are discussed in detail: the estimation of the uncertainty on the identified system parameters, and the use of an exogenous input in addition to the unmeasured operational excitation, for OMAX testing. In Section 5, the derivation of the modal parameters from the identified state-space model is treated, as well as the estimation of their probability density function. Finally, in Section 6, two real-life applications are discussed in detail.

2 State-space models of vibrating structures

2.1 Introduction

In this section, the use of a state-space model for operational modal analysis, with or without exogenous inputs, is discussed. Starting from a finite element description, that is commonly used for realistic physical modeling of structures in forward vibration problems, a state-space model, that is more convenient for solving inverse problems, is derived. This deterministic state-space model is then extended with unobserved inputs and output

disturbances, which are both modeled as stochastic quantities.

2.2 Linear dynamic finite element model

The finite element method is the most common tool for forward modeling of vibrating structures. In the case of a linear dynamic model with general viscous damping, one has the following system of ordinary differential equations:

$$\boldsymbol{M}\frac{d^2\boldsymbol{v}(t)}{dt^2} + \boldsymbol{C^v}\frac{d\boldsymbol{v}(t)}{dt} + \boldsymbol{K}\boldsymbol{v}(t) = \boldsymbol{B_{sel}}\boldsymbol{u}(t) \tag{1}$$

where $\boldsymbol{v}(t) \in \mathbb{R}^{n_{fe}}$ is the vector with nodal displacements, $\boldsymbol{M} \in \mathbb{R}^{n_{fe}\times n_{fe}}$, $\boldsymbol{C^v} \in \mathbb{R}^{n_{fe}\times n_{fe}}$ and $\boldsymbol{K} \in \mathbb{R}^{n_{fe}\times n_{fe}}$ are the mass, viscous damping, and stiffness matrices, respectively, and $\boldsymbol{B_{sel}} \in \mathbb{R}^{n_{fe}\times n_u}$ is a selection matrix such that the vector with externally applied forces, $\boldsymbol{u}(t) \in \mathbb{R}^{n_u}$, has only elements that are not identically zero.

2.3 Continuous-time state-space model

State-space equation. By rearranging (1) and assuming that $\boldsymbol{M}$ has full rank[1], a continuous-time state space model

$$\frac{d\boldsymbol{x}(t)}{dt} = \boldsymbol{A_c}\boldsymbol{x}(t) + \boldsymbol{B_c}\boldsymbol{u}(t), \tag{2}$$

where

$$\boldsymbol{x}(t) = \begin{bmatrix} \boldsymbol{v}(t) \\ \frac{d\boldsymbol{v}(t)}{dt} \end{bmatrix}$$
$$\boldsymbol{A_c} = \begin{bmatrix} \boldsymbol{0} & \boldsymbol{I} \\ -\boldsymbol{M}^{-1}\boldsymbol{K} & -\boldsymbol{M}^{-1}\boldsymbol{C^v} \end{bmatrix}$$
$$\boldsymbol{B_c} = \begin{bmatrix} \boldsymbol{0} \\ \boldsymbol{M}^{-1}\boldsymbol{B_{sel}} \end{bmatrix},$$

is obtained. The vector $\boldsymbol{x}(t) \in \mathbb{R}^n$ is called the *state* of the structure. The number of elements of $\boldsymbol{x}(t)$, n, is called the *model order*. If the state-space model is derived from a finite element model, as in this case, one has $n = 2n_{fe}$. When the state at $t = 0$ is known, the system of ordinary differential equations (2) can be solved for $\boldsymbol{x}(t)$:

$$\boldsymbol{x}(t) = e^{\boldsymbol{A_c}t}\boldsymbol{x}(0) + \int_{[0,t]} e^{\boldsymbol{A_c}(t-\tau)}\boldsymbol{B_c}\boldsymbol{u}(\tau)d\tau. \tag{3}$$

[1] In a beam model, for example, this implies that rotational inertia is included.

Input-output equation. If the output quantities of interest are linear combinations of nodal displacements, velocities or accelerations, one has

$$\begin{aligned}\boldsymbol{y}(t) &= \boldsymbol{C}_{\ddot{\boldsymbol{v}}}\frac{d^2\boldsymbol{v}(t)}{dt^2} + \boldsymbol{C}_{\dot{\boldsymbol{v}}}\frac{d\boldsymbol{v}(t)}{dt} + \boldsymbol{C}_{\boldsymbol{v}}\boldsymbol{v}(t) \\ &= \left[\begin{array}{c|c} \boldsymbol{C}_{\boldsymbol{v}} - \boldsymbol{C}_{\ddot{\boldsymbol{v}}}\boldsymbol{M}^{-1}\boldsymbol{K} & \boldsymbol{C}_{\dot{\boldsymbol{v}}} - \boldsymbol{C}_{\ddot{\boldsymbol{v}}}\boldsymbol{M}^{-1}\boldsymbol{C}^{\boldsymbol{v}} \end{array}\right] \boldsymbol{x}(t) + \boldsymbol{C}_{\ddot{\boldsymbol{v}}}\boldsymbol{M}^{-1}\boldsymbol{B}_{\boldsymbol{sel}}\boldsymbol{u}(t) \\ &= \boldsymbol{C}_{\boldsymbol{c}}\boldsymbol{x}(t) + \boldsymbol{D}_{\boldsymbol{c}}\boldsymbol{u}(t) \end{aligned} \tag{4}$$

where $\boldsymbol{C}_{\ddot{\boldsymbol{v}}} \in \mathbb{R}^{n_y \times n}$, $\boldsymbol{C}_{\dot{\boldsymbol{v}}} \in \mathbb{R}^{n_y \times n}$ and $\boldsymbol{C}_{\boldsymbol{v}} \in \mathbb{R}^{n_y \times n}$ are selection matrices. Finite strains can be included in $\boldsymbol{y}(t)$, since they can be obtained by dividing the difference between two displacement DOFs by the initial distance between their nodes.

Transfer function - poles. A Laplace transform of both sides of (2) and (4) leads to a parametrisation of the transfer function:

$$\boldsymbol{y}(s) = (\boldsymbol{C}_{\boldsymbol{c}}(s\boldsymbol{I} - \boldsymbol{A}_{\boldsymbol{c}})^{-1}\boldsymbol{B}_{\boldsymbol{c}} + \boldsymbol{D}_{\boldsymbol{c}})\boldsymbol{u}(s) = \boldsymbol{H}(s)\boldsymbol{u}(s). \tag{5}$$

Following Cramer's rule, one has

$$(s\boldsymbol{I} - \boldsymbol{A}_{\boldsymbol{c}})^{-1} = \frac{\mathrm{adj}(s\boldsymbol{I} - \boldsymbol{A}_{\boldsymbol{c}})}{\det(s\boldsymbol{I} - \boldsymbol{A}_{\boldsymbol{c}})},$$

where $\det(\square)$ denotes the determinant and $\mathrm{adj}(\square)$ the adjoint matrix of a square matrix $\square$. Since $\det(s\boldsymbol{I} - \boldsymbol{A}_{\boldsymbol{c}})$ is the characteristic polynomial of $\boldsymbol{A}_{\boldsymbol{c}}$, the poles of the transfer function are the eigenvalues of $\boldsymbol{A}_{\boldsymbol{c}}$.

Change of basis - decoupling. When the state is transformed to a new basis, $\boldsymbol{x} \mapsto \boldsymbol{T}^{-1}\boldsymbol{x}$ with $\boldsymbol{T} \in \mathbb{C}^{n \times n}$ nonsingular, the input-output map provided by the state-space description is preserved when $(\boldsymbol{A}_{\boldsymbol{c}}, \boldsymbol{B}_{\boldsymbol{c}}, \boldsymbol{C}_{\boldsymbol{c}}, \boldsymbol{D}_{\boldsymbol{c}}) \mapsto (\boldsymbol{T}^{-1}\boldsymbol{A}_{\boldsymbol{c}}\boldsymbol{T}, \boldsymbol{T}^{-1}\boldsymbol{B}_{\boldsymbol{c}}, \boldsymbol{C}_{\boldsymbol{c}}\boldsymbol{T}, \boldsymbol{D}_{\boldsymbol{c}})$, as follows from (2) and (4). In particular, when $\boldsymbol{A}_{\boldsymbol{c}}$ has a similarity transform,

$$\boldsymbol{A}_{\boldsymbol{c}} = \boldsymbol{\Psi}_{\boldsymbol{c}}\boldsymbol{\Lambda}_{\boldsymbol{c}}\boldsymbol{\Psi}_{\boldsymbol{c}}^{-1}, \tag{6}$$

with $\boldsymbol{\Lambda}_{\boldsymbol{c}}$ a diagonal matrix, (2) and (4) are decoupled by putting $\boldsymbol{T} = \boldsymbol{\Psi}_{\boldsymbol{c}}$:

$$\frac{d\boldsymbol{x}_{\boldsymbol{m}}(t)}{dt} = \boldsymbol{\Lambda}_{\boldsymbol{c}}\boldsymbol{x}_{\boldsymbol{m}}(t) + \boldsymbol{L}_{\boldsymbol{c}}^{T}\boldsymbol{u}(t) \tag{7}$$

$$\boldsymbol{y}(t) = \boldsymbol{\Phi}_{\boldsymbol{c}}\boldsymbol{x}_{\boldsymbol{m}}(t) + \boldsymbol{D}_{\boldsymbol{c}}\boldsymbol{u}(t). \tag{8}$$

The subscript m denotes *modal*, as will be explained shortly.

2.4 Discrete-time state-space model

Definition - ZOH assumption. Since for a given input $\boldsymbol{u}(t)$, solving the continuous-time state-space description analytically is usually impossible in the time domain, it seems natural to convert this model to discrete time:

$$\begin{aligned} \boldsymbol{x_{k+1}} &= \boldsymbol{A x_k} + \boldsymbol{B u_k} && (9) \\ \boldsymbol{y_k} &= \boldsymbol{C x_k} + \boldsymbol{D u_k}. && (10) \end{aligned}$$

For free vibration problems, where the inputs are identically zero, an exact discretisation is possible by solving the system of equations (2,4) using (3):

$$\begin{aligned} \boldsymbol{x}((k+1)T) &= e^{\boldsymbol{A_c}T}\boldsymbol{x}(kT) \\ \boldsymbol{y}(kT) &= \boldsymbol{C_c}\boldsymbol{x}(kT), \end{aligned}$$

where T denotes the sampling period. This leads to an exact map with $(\boldsymbol{A}, \boldsymbol{C}) = (e^{\boldsymbol{A_c}T}, \boldsymbol{C_c})$. The map is very important when solving the inverse modal analysis problem by fitting (9-10) to measured sampled data. When converting the fitted discrete-time state-space model to a continuous-time equivalent, the inverse map leads to the exact continuous-time equivalents of the discrete poles and mode shapes.

For forced vibration problems, a *Zero-Order-Hold* (ZOH) assumption is often made, which means that the force is assumed constant (equal to $\boldsymbol{u}(kT)$) in $[kT, (k+1)T)$. With this assumption, the following map is obtained from (3):

$$\begin{aligned} &\boldsymbol{A} = e^{\boldsymbol{A_c}T}, \quad \boldsymbol{B} = \int_{kT}^{(k+1)T} e^{\boldsymbol{A_c}((k+1)T-\tau)} d\tau \boldsymbol{B_c} = (\boldsymbol{A} - \boldsymbol{I})\boldsymbol{A_c}^{-1}\boldsymbol{B_c} \quad (11) \\ &\boldsymbol{C} = \boldsymbol{C_c}, \qquad \boldsymbol{D} = \boldsymbol{D_c}. \end{aligned}$$

A proof for the second equality in the expression for $\boldsymbol{B}$ can be found in (Juang, 1994, p. 20). Although alternative discretisation strategies are possible (Franklin et al., 1998, ch. 6), the ZOH discretisation has the advantage that it is exact when $\boldsymbol{u}(t) = \boldsymbol{0}$, as discussed above. However, the input matrix $\boldsymbol{B_c}$, that is calculated through the inverse map, is not a good approximation of the true $\boldsymbol{B_c}$ when the sampling frequency is not much larger than twice the largest important frequency that is present in the spectra of the input and output signals.

Solution of the state equations - impulse response. The state equations (9-10) can be solved by simple forward calculation:

$$\boldsymbol{y_k} = \boldsymbol{C}\boldsymbol{A}^k\boldsymbol{x_0} + \sum_{l=1}^{k} \boldsymbol{C}\boldsymbol{A}^{l-1}\boldsymbol{B}\boldsymbol{f_{k-l}} + \boldsymbol{D}\boldsymbol{f_k}.$$

From this result, the impulse response is readily obtained as

$$\boldsymbol{H_0} = \boldsymbol{D}, \qquad \boldsymbol{H_k} = \boldsymbol{C}\boldsymbol{A}^{k-1}\boldsymbol{B},\ k > 1. \tag{12}$$

Transfer function - poles. By taking the z-transform of both sides of (9-10), a parametrisation of the transfer function is obtained:

$$\boldsymbol{y}(z) = (\boldsymbol{C}(z\boldsymbol{I} - \boldsymbol{A})^{-1}\boldsymbol{B} + \boldsymbol{D})\boldsymbol{u}(z) = \boldsymbol{H}(z)\boldsymbol{u}(z) \tag{13}$$

Just as for the continuous-time state-space model (see Section 2.3), it follows from Cramer's rule that the poles of the transfer function are the eigenvalues of $\boldsymbol{A}$.

Change of basis - decoupling. Following the same lines as for the continuous-time case, one has that the input-output map provided by the discrete-time state-space description is preserved when $(\boldsymbol{A}, \boldsymbol{B}, \boldsymbol{C}, \boldsymbol{D}) \mapsto (\boldsymbol{T}^{-1}\boldsymbol{A}\boldsymbol{T}, \boldsymbol{T}^{-1}\boldsymbol{B}, \boldsymbol{C}\boldsymbol{T}, \boldsymbol{D})$, and that, when $\boldsymbol{A}$ has a similarity transform,

$$\boldsymbol{A} = \boldsymbol{\Psi_d}\boldsymbol{\Lambda_d}\boldsymbol{\Psi_d}^{-1}, \tag{14}$$

where $\boldsymbol{\Lambda_d}$ is a diagonal matrix, (9-10) is decoupled by putting $\boldsymbol{T} = \boldsymbol{\Psi_d}$:

$$\boldsymbol{x_{m,k+1}} = \boldsymbol{\Lambda_d}\boldsymbol{x_{m,k}} + \boldsymbol{L_d^T}\boldsymbol{u_k} \tag{15}$$

$$\boldsymbol{y_k} = \boldsymbol{\Phi_d}\boldsymbol{x_{m,k}} + \boldsymbol{D}\boldsymbol{u_k}. \tag{16}$$

2.5 Modeling loads and sensor noise

In this section, a step closer to the experimental world is made. The goal is to obtain a more realistic description for the *measured* input-output behavior of real structures. Therefore, measurement noise is taken into account, and the inputs $\boldsymbol{u}(t)$ that were considered in the previous section, are split into two parts: a part that can be measured in an operational vibration test, and a part that can not be measured.

Unobserved loads. When the loads can not be measured, they have to be identified together with the system, from the measured response. The concerned discipline is called output-only or blind system identification. When identifying the input and the system at the same time, a problem of identifiability occurs: the system can not be determined unless extra assumptions are made concerning the unknown inputs.

Most ambient excitation sources, such as seismic waves (Clough and Penzien, 1995), turbulent wind or water pressure (Durbin and Petterson Reif,

2001; Durbin and Medic, 2007), or road or railway traffic (Braun and Hellenbroich, 1991; ORE, 1971), are often modeled as stochastic loads in forward calculations. An exception is excitation due to rotating machinery, such as wind turbines, which usually has a harmonic nature, i.e., its frequency content consists approximately of discrete peaks that occur at integer multiples of a fundamental frequency.

When unobserved ambient or harmonic loads are taken into account during system identification, the presented model structures need to be extended. Pintelon et al. (2008) present a model for a structure's response to non-stationary harmonic excitation, and use it for operational modal analysis. This model is generally applicable and could be combined with the presented discrete-time state-space model. Stochastic load modeling is discussed in detail in the next paragraph.

Stationarity, ergodicity, and zero mean. When a system that is driven by an unmeasured, stochastic input, needs to be identified, extra assumptions on the input, that is, other that stochasticity, are needed. Wide-sense stationarity, which means that the covariance between two time samples depends only on the time difference, not on the time instances at which the samples were taken, and quadratic mean ergodicity, i.e., ensemble averaging can be replaced by time averaging, are classical assumptions (Dougherty, 1999). They are mild in the sense that if they are not valid, they only increase the variance errors of the identified system description. The zero mean assumption holds exactly when the constant trend is removed from the outputs (hence also from the unmeasured inputs) and from the measured inputs. In this case, the covariance functions of the inputs and outputs equal their correlation functions.

Discrete-time white noise. Another classical, but more restrictive assumption, is that the stochastic unobserved input is a white noise vector. The sampled, stationary stochastic input sequence $(\boldsymbol{u_k^s})$ is said to be a zero-mean discrete-time white noise sequence when its correlation function obeys (Dougherty, 1999, p. 154)

$$\boldsymbol{R_{u^s u^s,j}} = \mathcal{E}\left(\boldsymbol{u_{k+j}^s} \boldsymbol{u_k^{s\,T}}\right) = \begin{cases} \mathrm{Cov}(\boldsymbol{u_k^s}), & j = 0 \\ \boldsymbol{0}, & j \neq 0 \end{cases},$$

where $\mathcal{E}$ denotes the expectation operator and Cov the covariance operator. The discrete *Power Spectral Density* (PSD) of $(\boldsymbol{u_k^s})$, which is defined as the *Discrete Fourier Transform* (DFT) of $\boldsymbol{R_{u^s u^s,j}}$, obeys

$$\boldsymbol{S_{u^s u^s,j}} = \boldsymbol{R_{u^s u^s,0}}.$$

This means that the discrete PSD of a discrete-time white noise sequence is real and constant.

Colored noise. Whether the white noise assumption is approximately true for the unobserved stochastic inputs entirely depends on the PSD of the inputs in the considered frequency band. Often coloured noise is a more realistic assumption: the unobserved inputs are assumed to be white noise that has passed through a linear time-invariant system, called the noise colour. If in that case, white noise inputs are assumed, the noise colour of the unmeasured excitation is part of the identified system model (see Figure 1). It can only be separated from the true system model if some prior knowledge is available. For instance, if it can be assumed that the modes of the vibrating structure are lowly damped real normal modes, then highly damped and complex modes can be assumed to represent the input noise colour.

Sensor noise. Even if all inputs could be measured and the vibrating structure would obey all assumptions, that is, no model errors are made, there would still be a discrepancy between the *measured* inputs and outputs and their true values. This is due to electric disturbances in the measurement equipment. These disturbances can be important when the amplitudes of the measured signals are low compared to the noise floor of the equipment.

Based on physical principles, it can be shown that many important electr(on)ic disturbances have a white noise nature. Nyquist (1928) derived that at room temperature, the thermal noise voltage at both ends of a resistor is approximately white below 1000GHz. However, the measurement equipment makes up a dynamical system of its own, and the disturbances that it generates are not perfectly white. When nonwhite output measurement noise is modeled as white, the noise colour becomes part of the identified system, just as with nonwhite unmeasured inputs (see Figure 1). Harmonic measurement noise is often due to harmonic AC components in the electricity grid, and could be modeled just as harmonic unobserved loads.

2.6 A combined deterministic-stochastic state-space model

Continuous combined state-space model. When the observed (deterministic) inputs $\boldsymbol{u}(t)$ and outputs $\boldsymbol{y}(t)$ are corrupted by additive sensor noise, denoted as $\boldsymbol{u^n}(t) \in \mathbb{R}^{n_u}$ and $\boldsymbol{y^n}(t) \in \mathbb{R}^{n_y}$, respectively, and when unobserved stochastic inputs $\boldsymbol{u^s}(t) \in \mathbb{R}^{n_u^s}$ are present, the state-space model

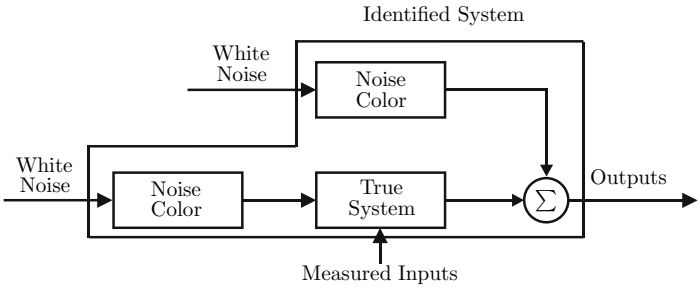

Figure 1. Block diagram of the identified system description when the unmeasured excitation is coloured noise.

(2, 4) can be extended to

$$\frac{d\boldsymbol{x}(t)}{dt} = \boldsymbol{A_c}\boldsymbol{x}(t) + \boldsymbol{B_c}\boldsymbol{u}(t) + \boldsymbol{w}(t) \tag{17}$$

$$\boldsymbol{y}(t) = \boldsymbol{C_c}\boldsymbol{x}(t) + \boldsymbol{D_c}\boldsymbol{u}(t) + \boldsymbol{v}(t), \tag{18}$$

where

$$\boldsymbol{w}(t) \triangleq \boldsymbol{B_c^s}\boldsymbol{u^s}(t) - \boldsymbol{B_c}\boldsymbol{u^n}(t), \qquad \boldsymbol{v}(t) \triangleq \boldsymbol{D_c^s}\boldsymbol{u^s}(t) - \boldsymbol{D_c}\boldsymbol{u^n}(t) + \boldsymbol{y^n}(t), \tag{19}$$

$$\boldsymbol{B_c^s} = \begin{bmatrix} \boldsymbol{0} \\ \boldsymbol{M}^{-1}\boldsymbol{B_{sel2}} \end{bmatrix}, \qquad \text{and} \qquad \boldsymbol{D_c^s} = \boldsymbol{C_{\ddot{v}}}\boldsymbol{M}^{-1}\boldsymbol{B_{sel2}},$$

with $\boldsymbol{B_{sel2}} \in \mathbb{R}^{n_{fe} \times n_u^s}$ a selection matrix.

Discrete combined state-space model - decomposition. With a discretisation scheme such as ZOH, (17-18) can be converted to

$$\boldsymbol{x_{k+1}} = \boldsymbol{A}\boldsymbol{x_k} + \boldsymbol{B}\boldsymbol{u_k} + \boldsymbol{w_k} \tag{20}$$

$$\boldsymbol{y_k} = \boldsymbol{C}\boldsymbol{x_k} + \boldsymbol{D}\boldsymbol{u_k} + \boldsymbol{v_k}. \tag{21}$$

When it is assumed that the samples of $\boldsymbol{u^n}(t)$, $\boldsymbol{y^n}(t)$, and $\boldsymbol{u^s}(t)$ make up discrete-time white noise sequences, $\boldsymbol{w_k}$ and $\boldsymbol{v_k}$ are discrete-time white noise sequences as well:

$$\mathcal{E}\left(\begin{bmatrix} \boldsymbol{w_{k+l}} \\ \boldsymbol{v_{k+l}} \end{bmatrix} \begin{bmatrix} \boldsymbol{w_k} \\ \boldsymbol{v_k} \end{bmatrix}^T\right) = \begin{bmatrix} \boldsymbol{Q} & \boldsymbol{S} \\ \boldsymbol{S}^T & \boldsymbol{R} \end{bmatrix} \delta_1(l), \tag{22}$$

where $\delta_1(\square)$ is the unit impulse function, i.e., $\delta_1(0) = 1$ and $\delta_1(\square) = 0$ if $\square \neq 0$. With the decomposition of the states and outputs in a deterministic and a stochastic part,

$$\boldsymbol{x_k} = \boldsymbol{x_k^d} + \boldsymbol{x_k^s} \qquad \text{and} \qquad \boldsymbol{y_k} = \boldsymbol{y_k^d} + \boldsymbol{y_k^s},$$

(20-20) is decomposed into a deterministic subsystem

$$\begin{aligned} \boldsymbol{x_{k+1}^d} &= \boldsymbol{A x_k^d} + \boldsymbol{B u_k} && (23) \\ \boldsymbol{y_k^d} &= \boldsymbol{C x_k^d} + \boldsymbol{D u_k}, && (24) \end{aligned}$$

and a stochastic subsystem

$$\begin{aligned} \boldsymbol{x_{k+1}^s} &= \boldsymbol{A x_k^s} + \boldsymbol{w_k} && (25) \\ \boldsymbol{y_k^s} &= \boldsymbol{C x_k^s} + \boldsymbol{v_k}. && (26) \end{aligned}$$

Just as for the deterministic subsystem, the eigenvalue decomposition of $\boldsymbol{A}$, (14), decouples the stochastic subsystem:

$$\begin{aligned} \boldsymbol{x_{m,k+1}^s} &= \boldsymbol{\Lambda_d x_{m,k}^s} + \boldsymbol{w_{m,k}} && (27) \\ \boldsymbol{y_k^s} &= \boldsymbol{\Phi_d x_{m,k}^s} + \boldsymbol{v_{m,k}}, && (28) \end{aligned}$$

where $\boldsymbol{w_{m,k}} = \boldsymbol{\Psi_d^{-1}} \boldsymbol{w_k}$.

Correlation matrices. The following definitions of correlation matrices of the stochastic subsystem (25-26) and the relationships between them are very frequently used, both in solving forward and inverse problems:

$$\begin{aligned} \boldsymbol{\Sigma^s} &\triangleq \mathcal{E}\left(\boldsymbol{x_{k+1}^s} {\boldsymbol{x_{k+1}^s}}^T\right) = \mathcal{E}\left(\left(\boldsymbol{A x_k^s} + \boldsymbol{w_k}\right)\left(\boldsymbol{A x_k^s} + \boldsymbol{w_k}\right)^T\right) \\ &= \boldsymbol{A \Sigma^s A}^T + \boldsymbol{Q} && (29) \\ \boldsymbol{G} &\triangleq \mathcal{E}\left(\boldsymbol{x_{k+1}^s} {\boldsymbol{y_k^s}}^T\right) = \mathcal{E}\left(\left(\boldsymbol{A x_k^s} + \boldsymbol{w_k}\right)\left(\boldsymbol{C x_k^s} + \boldsymbol{v_k}\right)^T\right) \\ &= \boldsymbol{A \Sigma^s C}^T + \boldsymbol{S} && (30) \\ \boldsymbol{\Lambda_l} &\triangleq \mathcal{E}\left(\boldsymbol{y_{k+l}^s} {\boldsymbol{y_k^s}}^T\right) \\ &= \begin{cases} \mathcal{E}\left(\left(\boldsymbol{C x_k^s} + \boldsymbol{v_k}\right)\left(\boldsymbol{C x_k^s} + \boldsymbol{v_k}\right)^T\right) = \boldsymbol{C \Sigma^s C}^T + \boldsymbol{R}, & l = 0 \\ \mathcal{E}\left(\left(\boldsymbol{C x_{k+l}^s} + \boldsymbol{v_{k+l}}\right) {\boldsymbol{y_k^s}}^T\right) = \boldsymbol{C A}^{l-1} \boldsymbol{G}, & l > 0 \\ \mathcal{E}\left(\boldsymbol{y_k^s} {\boldsymbol{y_{k+l}^s}}^T\right)^T = \boldsymbol{G}^T \left(\boldsymbol{A}^{l-1}\right)^T \boldsymbol{C}^T, & l < 0 \end{cases} && (31) \end{aligned}$$

where, as before, stationarity and ergodicity of all stochastic sequences was assumed, as well as the fact that $\boldsymbol{x_k}$ is independent of $\boldsymbol{w_k}$ and $\boldsymbol{v_k}$, which follows immediately from equations (20-21).

Positive output correlation function and positive output power spectral density. When comparing (12) and (31), it follows that the impulse response function of the deterministic subsystem (23-24) and the positive output correlation function of the stochastic subsystem (25-26) have the same structure: the quadruplet $(\boldsymbol{A}, \boldsymbol{G}, \boldsymbol{C}, \boldsymbol{\Lambda_0}/2)$ of the stochastic positive correlation function plays the role of the quadruplet $(\boldsymbol{A}, \boldsymbol{B}, \boldsymbol{C}, \boldsymbol{D})$ of the deterministic impulse response function. Since the transfer function of the deterministic subsystem is the z-transform of its impulse response function and the positive power spectral density of the stochastic subsystem is the z-transform of its positive correlation function, it follows from (13) that

$$\boldsymbol{S}^{+}_{\boldsymbol{y^s y^s}}(z) = \boldsymbol{C}(z\boldsymbol{I} - \boldsymbol{A})^{-1}\boldsymbol{G} + \frac{1}{2}\boldsymbol{\Lambda_0}. \tag{32}$$

State estimation - the reference-based Kalman filter. Because the stochastic terms $\boldsymbol{w_k}$ and $\boldsymbol{v_k}$ are unknown, the state $\boldsymbol{x_k}$ cannot be calculated exactly from (20-21). Nevertheless, a one-step ahead estimate of $\boldsymbol{x^s_{k+1}}$ can be calculated if the current output vector $\boldsymbol{y_k}$ is known. From $\boldsymbol{y_k}$, $\boldsymbol{y^s_k}$ is obtained after subtracting the deterministic part $\boldsymbol{y^d_k}$. The Kalman filter offers a technique for determining the optimal linear estimate because the estimator is unbiased and has minimum variance (Kalman, 1960).

Reynders and De Roeck (2008) worked out a reference-based Kalman filter. Reference outputs form a subset (containing n_r elements) of the complete set of n_y outputs:

$$\boldsymbol{y^{ref}_k} \quad \triangleq \quad \boldsymbol{S^r y_k},$$

where $\boldsymbol{S^r} \in \mathbb{N}^{n_r \times n_y}$ is a selection matrix. In order not to lose information, it is important that any mode of interest is clearly present in at least one reference output. Good reference output candidates are usually driving point outputs, or, in case of measurements performed in different setups, the output channels common to each setup. The reference outputs can be written as

$$\boldsymbol{y^{ref}_k} = \boldsymbol{S^r C x_k} + \boldsymbol{S^r D u_k} + \boldsymbol{S^r v_k} \triangleq \boldsymbol{C^{ref} x_k} + \boldsymbol{D^{ref} u_k} + \boldsymbol{v^{ref}_k}.$$

Reynders and De Roeck (2008) showed that the optimal linear one-step-ahead state estimate $\boldsymbol{\hat{x}^s_{k+1}}$ and the reference-based non-stationary Kalman filter $\boldsymbol{K_k}$ can be calculated from the following set of equations, using the current state estimate $\boldsymbol{\hat{x}^s_k}$ and the measured current reference output vector

$\boldsymbol{y_k^{s,ref}}$ and assuming $\hat{\boldsymbol{x}}_{\boldsymbol{0}}^{\boldsymbol{s}} = \mathcal{E}\left(\boldsymbol{x}_{\boldsymbol{0}}^{\boldsymbol{s}}\right)$:

$$\begin{aligned}
\hat{\boldsymbol{x}}_{\boldsymbol{k+1}}^{\boldsymbol{s}} &= (\boldsymbol{A} - \boldsymbol{K_k}\boldsymbol{C}^{\boldsymbol{ref}})\hat{\boldsymbol{x}}_{\boldsymbol{k}}^{\boldsymbol{s}} + \boldsymbol{K_k}\boldsymbol{y}_{\boldsymbol{k}}^{\boldsymbol{s,ref}} && (33)\\
\boldsymbol{K_k} &= (\boldsymbol{A}\boldsymbol{P_k}\boldsymbol{C}^{\boldsymbol{ref}\,T} + \boldsymbol{S}^{\boldsymbol{ref}})(\boldsymbol{R}^{\boldsymbol{ref}} + \boldsymbol{C}^{\boldsymbol{ref}}\boldsymbol{P_k}\boldsymbol{C}^{\boldsymbol{ref}\,T})^{-1} && (34)\\
\boldsymbol{P_{k+1}} &= \boldsymbol{A}\boldsymbol{P_k}\boldsymbol{A}^T + \boldsymbol{Q} - (\boldsymbol{A}\boldsymbol{P_k}\boldsymbol{C}^{\boldsymbol{ref}\,T} + \boldsymbol{S}^{\boldsymbol{ref}}) \\
&\quad \cdot(\boldsymbol{R}^{\boldsymbol{ref}} + \boldsymbol{C}^{\boldsymbol{ref}}\boldsymbol{P_k}\boldsymbol{C}^{\boldsymbol{ref}\,T})^{-1}(\boldsymbol{A}\boldsymbol{P_k}\boldsymbol{C}^{\boldsymbol{ref}\,T} + \boldsymbol{S}^{\boldsymbol{ref}})^T && (35)
\end{aligned}$$

where $\boldsymbol{R}^{\boldsymbol{ref}} = \boldsymbol{S}^{\boldsymbol{r}}\boldsymbol{R}\boldsymbol{S}^{\boldsymbol{r}\,T}$, $\boldsymbol{S}^{\boldsymbol{ref}} = \boldsymbol{S}\boldsymbol{S}^{\boldsymbol{r}\,T}$ and $\boldsymbol{P_k}$ is correlation of the state estimation error:

$$\boldsymbol{e_k} \triangleq \boldsymbol{x_k} - \hat{\boldsymbol{x}}_{\boldsymbol{k}} = \boldsymbol{x}_{\boldsymbol{k}}^{\boldsymbol{s}} - \hat{\boldsymbol{x}}_{\boldsymbol{k}}^{\boldsymbol{s}}, \qquad \boldsymbol{P_k} \triangleq \mathcal{E}\left(\boldsymbol{e_k}\boldsymbol{e}_{\boldsymbol{k}}^T\right). \tag{36}$$

After solving (35) for $\boldsymbol{P_k}$, $\boldsymbol{K_k}$ can be calculated with (34), and the optimal estimate of $\hat{\boldsymbol{x}}_{\boldsymbol{k+1}}$ is then obtained using (33). It is usually assumed that $\hat{\boldsymbol{x}}_{\boldsymbol{0}}^{\boldsymbol{s}} = \boldsymbol{0}$ and $\boldsymbol{P_0} = \boldsymbol{0}$, see Van Overschee and De Moor (1996), but other choices can be made.

Since the stochastic part of the model (20-21) is driven by stationary random processes, the Kalman filter $\boldsymbol{K_k}$ is equal to the time-invariant matrix $\boldsymbol{K}$ when no initial conditions are taken into account (as is the case when taking a double-sided z transform), which is formally shown in (Anderson and Moore, 1979, ch. 4). In this case, $\boldsymbol{P_k}$ equals the time-invariant matrix $\boldsymbol{P}$, and the subscript k in (34) and (35) disappears. Since the effect of initial conditions dies out for a stable system when $k \to \infty$, it also follows that $\boldsymbol{K_k} \to \boldsymbol{K},\ k \to \infty$.

Reference-based forward innovation model. The (reference-based) forward innovation $\boldsymbol{e}_{\boldsymbol{k}}^{\boldsymbol{(ref),f}}$ is defined as

$$\boldsymbol{e}_{\boldsymbol{k}}^{\boldsymbol{(ref),f}} \triangleq \boldsymbol{y}_{\boldsymbol{k}}^{\boldsymbol{(ref)}} - \boldsymbol{C}^{\boldsymbol{(ref)}}\hat{\boldsymbol{x}}_{\boldsymbol{k}} - \boldsymbol{D}^{\boldsymbol{(ref)}}\boldsymbol{u_k}.$$

By decomposing the Kalman filter state $\hat{\boldsymbol{x}}_{\boldsymbol{k+1}}$ into its deterministic and stochastic components, one has

$$\begin{aligned}
\hat{\boldsymbol{x}}_{\boldsymbol{k+1}} &= \boldsymbol{x}_{\boldsymbol{k+1}}^{\boldsymbol{d}} + \hat{\boldsymbol{x}}_{\boldsymbol{k+1}}^{\boldsymbol{s}} = \boldsymbol{A}\boldsymbol{x}_{\boldsymbol{k}}^{\boldsymbol{d}} + \boldsymbol{B}\boldsymbol{u_k} + (\boldsymbol{A} - \boldsymbol{K_k}\boldsymbol{C}^{\boldsymbol{ref}})\hat{\boldsymbol{x}}_{\boldsymbol{k}}^{\boldsymbol{s}} + \boldsymbol{K_k}\boldsymbol{y}_{\boldsymbol{k}}^{\boldsymbol{ref,s}} \\
&= \boldsymbol{A}\hat{\boldsymbol{x}}_{\boldsymbol{k}} + \boldsymbol{B}\boldsymbol{u_k} + \boldsymbol{K_k}(\boldsymbol{y}_{\boldsymbol{k}}^{\boldsymbol{ref}} - \boldsymbol{C}^{\boldsymbol{ref}}\hat{\boldsymbol{x}}_{\boldsymbol{k}} - \boldsymbol{D}^{\boldsymbol{ref}}\boldsymbol{u_k}) \\
&= \boldsymbol{A}\hat{\boldsymbol{x}}_{\boldsymbol{k}} + \boldsymbol{B}\boldsymbol{u_k} + \boldsymbol{K_k}\boldsymbol{S}^{\boldsymbol{r}}\boldsymbol{e}_{\boldsymbol{k}}^{\boldsymbol{f}}, && (37)
\end{aligned}$$

where the second equality follows from (33). Obviously, one has

$$\begin{aligned}
\boldsymbol{y_k} &= \boldsymbol{C}\hat{\boldsymbol{x}}_{\boldsymbol{k}} + \boldsymbol{D}\boldsymbol{u_k} + (\boldsymbol{y_k} - \boldsymbol{C}\hat{\boldsymbol{x}}_{\boldsymbol{k}} - \boldsymbol{D}\boldsymbol{u_k}) \\
&= \boldsymbol{C}\hat{\boldsymbol{x}}_{\boldsymbol{k}} + \boldsymbol{D}\boldsymbol{u_k} + \boldsymbol{e}_{\boldsymbol{k}}^{\boldsymbol{f}}. && (38)
\end{aligned}$$

Equations (37-38) represent the reference-based forward innovation model of the structure. It follows that for large k, the Kalman filter states constitute a particular state-space basis, since when $k \to \infty$, $\boldsymbol{K_k} \to \boldsymbol{K}$ as explained above, and $(\boldsymbol{K S^r e_k^f})$ and $(\boldsymbol{e_k^f})$ are system and measurement noise sequences, respectively, that obey the discrete-time white noise assumption.

3 Subspace identification: principles and strategies

3.1 Introduction

System Identification can be defined as the field of study where models are fitted to measured data. It involves three basic entities (Ljung, 1999, p. 13):

- designing an experiment that is as informative as possible and obtaining the data;
- choosing a set of candidate models, like for instance a stochastic state space model structure;
- choosing an identification method, i.e., a strategy for determining the model in the set that explains the data 'best', and an identification algorithm, i.e., a numerical algorithm that calculates the actual estimate.

A myriad of system identification algorithms is available from the literature, but, as shown by Ljung (1999), they can be considered as particular implementations of just a few general ideas. This section introduces the main ideas that lie behind the class of subspace identification algorithms for fitting the discrete-time state-space model of a vibrating structure, presented in the previous section, to measured data.

In the remainder of this chapter, the following assumptions are made.

Assumption 3.1. The stochastic output sequence $\boldsymbol{y_k^s}$ is generated by (25-26). The white process and measurement noise sequences are not identically zero.

Assumption 3.2. When exogenous forces are measured, the force sequence $(\boldsymbol{u_k}), k = 0, \ldots, N-1$, is observed free of noise and it is persistently exciting of order $\geq 2\imath + n$. The latter is a technical assumption which ensures that a block Hankel input matrix with $2\imath + n$ block rows has full row rank. The response sequence $(\boldsymbol{y_k^d})$ due to the input sequence $(\boldsymbol{u_k})$ is generated by the deterministic subsystem (23-24), which is controllable.

Assumption 3.3. When exogenous forces are measured, they are uncorrelated with the stochastic outputs, i.e.,

$$\forall k, l : \mathcal{E}\left(\boldsymbol{y_k^s u_l^T}\right) = \boldsymbol{0}.$$

3.2 System realisation

Introduction. The realisation problem was originally defined by Kalman (1963) as the problem of identifying a linear dynamic system from a non-parametric impulse response sequence that was generated by this system. Ho and Kalman (1966) found an efficient way to solve this problem, beginning with a finite-dimensional block Hankel matrix composed of noise-free impulse responses and ending with the system matrices of a deterministic state-space model. Later, Zeiger and McEwen (1974) and Kung (1978) proposed to perform the factorisation step of the Ho-Kalman procedure by singular value decomposition, where only the significant singular values and the corresponding singular vectors are retained. This truncation enabled one to deal with noise on the impulse responses, which is always present in experimental data. Another variant called the *Eigensystem Realisation Algorithm* (ERA), developed by Juang and Pappa (1985), introduced the idea of reference outputs into the realisation procedure. Later, Juang et al. (1988) proposed a variant of ERA that starts from correlations of impulse responses instead of the impulse response matrices themselves. This version is called the ERA with data correlations (ERA/DC). Akaike (1974) extended the realisation theory to stochastic systems and also gave a stochastic interpretation of the Ho-Kalman algorithm.

Stochastic system realisation. Suppose a nonparametric estimate of the stochastic output correlation sequence ($\boldsymbol{\Lambda_k^{ref}}$) is available. From (31), it follows that these correlation matrices can be parametrised as follows:

$$\boldsymbol{\Lambda_k^{ref}} = \boldsymbol{C}\boldsymbol{A}^{k-1}\boldsymbol{G^{ref}},\ k \geq 1.$$

Stochastic realisation starts with gathering the correlation matrices in a block Hankel matrix:

$$\boldsymbol{L_{1|\imath}^{ref}} \triangleq \begin{bmatrix} \boldsymbol{\Lambda_1^{ref}} & \boldsymbol{\Lambda_2^{ref}} & \dots & \boldsymbol{\Lambda_\imath^{ref}} \\ \boldsymbol{\Lambda_2^{ref}} & \boldsymbol{\Lambda_3^{ref}} & \dots & \boldsymbol{\Lambda_{\imath+1}^{ref}} \\ \vdots & \vdots & \dots & \vdots \\ \boldsymbol{\Lambda_\imath^{ref}} & \boldsymbol{\Lambda_{\imath+1}^{ref}} & \dots & \boldsymbol{\Lambda_{2\imath-1}^{ref}} \end{bmatrix}, \tag{39}$$

where $\imath$ is chosen in such a way that, if n is the expected system order, $n_y\imath \geq n$, $n_r\imath \geq n$ and $\imath \geq 2$. The block Hankel matrix decomposes into the extended observability matrix $\boldsymbol{\mathcal{O}_\imath}$ and the reference-based extended stochas-

tic controllability matrix $\boldsymbol{\mathcal{C}_i^S} \in \mathbb{R}^{n_y \times \imath n_r}$:

$$\boldsymbol{L_{1|\imath}^{ref}} = \underbrace{\begin{bmatrix} \boldsymbol{C} \\ \boldsymbol{CA} \\ \dots \\ \boldsymbol{CA}^{\imath-1} \end{bmatrix}}_{=\boldsymbol{\mathcal{O}_\imath}} \underbrace{\begin{bmatrix} \boldsymbol{G^{ref}} & \boldsymbol{AG^{ref}} & \dots & \boldsymbol{A}^{\imath-1}\boldsymbol{G^{ref}} \end{bmatrix}}_{\triangleq \boldsymbol{\mathcal{C}_i^S}}. \tag{40}$$

The matrices $\boldsymbol{\mathcal{O}_\imath}$ and $\boldsymbol{\mathcal{C}_i^S}$ can be obtained from $\boldsymbol{L_{1|\imath}^{ref}}$, up to a similarity transformation of the $\boldsymbol{A}$ matrix, using reduced singular value decomposition:

$$\boldsymbol{L_{1|\imath}^{ref}} = \boldsymbol{USV}^T, \qquad \boldsymbol{\mathcal{O}_\imath} = \boldsymbol{US}^{1/2}, \qquad \boldsymbol{\mathcal{C}_i^S} = \boldsymbol{S}^{1/2}\boldsymbol{V}^T, \tag{41}$$

where $\boldsymbol{S} \in \mathbb{R}^{n \times n}$ contains only the nonzero singular values and $\boldsymbol{U} \in \mathbb{R}^{\imath n_y \times n}$ and $\boldsymbol{V} \in \mathbb{R}^{\imath n_r \times n}$ contain the corresponding singular vectors. If the stochastic output correlation matrices $\boldsymbol{\Lambda_k^{ref}}$ are exact, the number of nonzero singular values equals the system order n. If not, the system order is lower than the number of nonzero singular values. It then needs to be estimated as the number of significant singular values. In this case $\boldsymbol{S}$ contains only the significant singular values and $\boldsymbol{U}$ and $\boldsymbol{V}$ contain the corresponding singular vectors.

The $\boldsymbol{C}$ matrix can be determined as the first n_y rows of $\boldsymbol{\mathcal{O}_\imath}$ and the $\boldsymbol{G^{ref}}$ matrix can be determined as the first n_r columns of $\boldsymbol{\mathcal{C}_\imath}$. Different algorithms have been proposed for the determination of $\boldsymbol{A}$. The algorithm of Kung (1978) is computationally the most efficient one. It makes use of the shift structure of the matrix $\boldsymbol{\mathcal{O}_\imath}$:

$$\boldsymbol{A} = \underline{\boldsymbol{\mathcal{O}_i}}^{\dagger} \overline{\boldsymbol{\mathcal{O}_i}}. \tag{42}$$

where $\underline{\boldsymbol{\mathcal{O}_\imath}}$ is equal to $\boldsymbol{\mathcal{O}_\imath}$ without the last n_y rows and $\overline{\boldsymbol{\mathcal{O}_\imath}}$ is equal to $\boldsymbol{\mathcal{O}_\imath}$ without the first n_y rows. $\square^\dagger$ denotes the Moore-Penrose pseudo-inverse of the matrix $\square$, see Ben-Israel and Greville (1974).

3.3 Subspace identification

Introduction. As shown in this section, subspace identification can be considered as an extension of system realisation. Instead of starting from a nonparametric impulse response or stochastic correlation function, subspace methods start directly from the measured data samples, which are put in different Hankel matrices. Projections between the data Hankel matrices then lead to a matrix from which the extended observability matrix $\boldsymbol{\mathcal{O}_\imath}$ is derived by performing a singular value decomposition, just as in the system

realisation technique discussed above. In a second step, the state-space matrices are identified using $\boldsymbol{\mathcal{O}_i}$. Several algorithms exist for this, and some of them are discussed in the next section. The discussion hereunder is restricted to the time domain, but as shown by Cauberghe (2004), the same techniques can be employed starting from frequency-domain data.

Orthogonal and oblique projections. Subspace identification methods make extensive use of geometric projections. This paragraph provides a concise review on the topic. Consider the matrices $\boldsymbol{M_1} \in \mathbb{R}^{m_1 \times \jmath}$, $\boldsymbol{M_2} \in \mathbb{R}^{m_2 \times \jmath}$ and $\boldsymbol{M_3} \in \mathbb{R}^{m_3 \times \jmath}$. The row space spanned by the rows of $\boldsymbol{M_2}$, denoted as $\mathcal{M}_2$, is defined as the set of all possible linear combinations of the rows of $\boldsymbol{M_2}$:

$$\mathcal{M}_2 \triangleq \left\{ \boldsymbol{y} \in \mathbb{R}^{\jmath} | \boldsymbol{y} = \boldsymbol{M_2}^T \boldsymbol{x},\ \forall \boldsymbol{x} \in \mathbb{R}^{m_2} \right\}.$$

The orthogonal projection of $\boldsymbol{M_1}$ onto $\mathcal{M}_2$ is defined as

$$\boldsymbol{M_1}/\mathcal{M}_2 \triangleq \boldsymbol{M_1}\boldsymbol{M_2}^T \left(\boldsymbol{M_2}\boldsymbol{M_2}^T\right)^{\dagger} \boldsymbol{M_2}.$$

When $\boldsymbol{M_1}/\mathcal{M}_2 = \boldsymbol{0}$, the rows of $\boldsymbol{M_1}$ and $\boldsymbol{M_2}$ are said to be orthogonal to each other. The orthogonal projection $\boldsymbol{M_1}/\mathcal{M}_2$ is graphically depicted in Figure 2 for $m_1 = m_2 = 1$ and $\jmath = 2$.

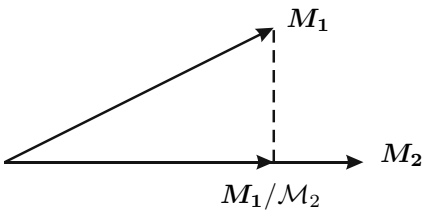

Figure 2. The orthogonal projection of $\boldsymbol{M_1}$ on the row space of $\boldsymbol{M_2}$, for the case $m_1 = m_2 = 1$ and $\jmath = 2$.

The oblique projection of $\boldsymbol{M_1}$ onto $\mathcal{M}_2$ along the row space of $\boldsymbol{M_3}$, denoted as $\mathcal{M}_3$, is defined as

$$\boldsymbol{M_1}/_{\mathcal{M}_3}\mathcal{M}_2 \triangleq \boldsymbol{M_1} \begin{bmatrix} \boldsymbol{M_2} \\ \boldsymbol{M_3} \end{bmatrix}^T \left(\begin{bmatrix} \boldsymbol{M_2} \\ \boldsymbol{M_3} \end{bmatrix} \begin{bmatrix} \boldsymbol{M_2} \\ \boldsymbol{M_3} \end{bmatrix}^T \right)^{\dagger} \begin{bmatrix} \boldsymbol{M_2} \\ \boldsymbol{0} \end{bmatrix}.$$

From the definition, it follows immediately that $\boldsymbol{M_3}/_{\mathcal{M}_3}\mathcal{M}_2 = \boldsymbol{0}$. The oblique projection $\boldsymbol{M_1}/_{\mathcal{M}_3}\mathcal{M}_2$ is graphically depicted in Figure 3 for $m_1 = m_2 = m_3 = 1$ and $\jmath = 2$.

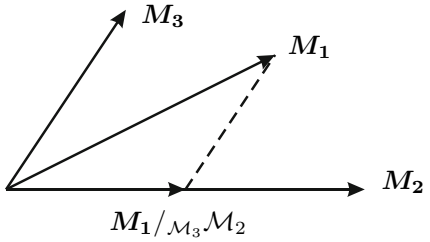

Figure 3. The oblique projection of $\boldsymbol{M_1}$ on the row space of $\boldsymbol{M_2}$ along $\boldsymbol{M_3}$, for the case $m_1 = m_2 = m_3 = 1$ and $\jmath = 2$.

Matrix input-output equations. From (23-24), one has the following relationship for the deterministic subsystem of a combined deterministic-stochastic state-space model:

$$\begin{bmatrix} \boldsymbol{y_0^d} \\ \boldsymbol{y_1^d} \\ \vdots \\ \boldsymbol{y_{\imath-1}^d} \end{bmatrix} = \underbrace{\begin{bmatrix} \boldsymbol{C} \\ \boldsymbol{CA} \\ \vdots \\ \boldsymbol{CA^{\imath-1}} \end{bmatrix}}_{=\boldsymbol{\mathcal{O}_\imath}} \boldsymbol{x_0^d} + \underbrace{\begin{bmatrix} \boldsymbol{D} & \boldsymbol{0} & \dots & \boldsymbol{0} \\ \boldsymbol{CB} & \boldsymbol{D} & \dots & \boldsymbol{0} \\ \vdots & \vdots & \dots & \boldsymbol{0} \\ \boldsymbol{CA^{\imath-2}B} & \boldsymbol{CA^{\imath-3}B} & \dots & \boldsymbol{D} \end{bmatrix}}_{\triangleq \boldsymbol{\mathcal{F}_\imath^d}} \begin{bmatrix} \boldsymbol{u_0} \\ \boldsymbol{u_1} \\ \vdots \\ \boldsymbol{u_\imath} \end{bmatrix}. \quad (43)$$

Define a block Hankel matrix of outputs as

$$\boldsymbol{Y_{k_1|k_2}} \triangleq \begin{bmatrix} \boldsymbol{y_{k_1}} & \boldsymbol{y_{k_1+1}} & \cdots & \boldsymbol{y_{k_1+\jmath-1}} \\ \boldsymbol{y_{k_1+1}} & \boldsymbol{y_{k_1+2}} & \cdots & \boldsymbol{y_{k_1+\jmath}} \\ \vdots & \vdots & \dots & \vdots \\ \boldsymbol{y_{k_2}} & \boldsymbol{y_{k_2+1}} & \cdots & \boldsymbol{y_{k_2+\jmath-1}} \end{bmatrix},$$

a block Hankel matrix of inputs as

$$\boldsymbol{U_{k_1|k_2}} \triangleq \begin{bmatrix} \boldsymbol{u_{k_1}} & \boldsymbol{u_{k_1+1}} & \cdots & \boldsymbol{u_{k_1+\jmath-1}} \\ \boldsymbol{u_{k_1+1}} & \boldsymbol{u_{k_1+2}} & \cdots & \boldsymbol{u_{k_1+\jmath}} \\ \vdots & \vdots & \dots & \vdots \\ \boldsymbol{u_{k_2}} & \boldsymbol{u_{k_2+1}} & \cdots & \boldsymbol{u_{k_2+\jmath-1}} \end{bmatrix},$$

and a block row vector of states as

$$\boldsymbol{X_{k_1|k_1}} \triangleq \begin{bmatrix} \boldsymbol{x_{k_1}} & \boldsymbol{x_{k_1+1}} & \dots & \boldsymbol{x_{k_1+\jmath-1}} \end{bmatrix}.$$

With these definitions, (43) generalises to

$$\boldsymbol{Y}_{\boldsymbol{k_1|k_2}} = \boldsymbol{\mathcal{O}}_{\boldsymbol{k_2-k_1+1}} \boldsymbol{X}^{\boldsymbol{d}}_{\boldsymbol{k_1|k_1}} + \boldsymbol{\mathcal{F}}^{\boldsymbol{d}}_{\boldsymbol{i}} \boldsymbol{U}_{\boldsymbol{k_1|k_2}} + \boldsymbol{Y}^{\boldsymbol{s}}_{\boldsymbol{k_1|k_2}}, \tag{44}$$

where $\boldsymbol{Y}^{\boldsymbol{s}}_{\boldsymbol{k_1|k_2}}$ denotes the stochastic part of $\boldsymbol{Y}_{\boldsymbol{k_1|k_2}}$ and $\boldsymbol{X}^{\boldsymbol{d}}_{\boldsymbol{k_1|k_1}}$ the deterministic part of $\boldsymbol{X}_{\boldsymbol{k_1|k_1}}$. As a special case, one has

$$\boldsymbol{Y}_{\boldsymbol{i|2i-1}} = \boldsymbol{\mathcal{O}}_{\boldsymbol{i}} \boldsymbol{X}^{\boldsymbol{d}}_{\boldsymbol{i|i}} + \boldsymbol{\mathcal{F}}^{\boldsymbol{d}}_{\boldsymbol{i}} \boldsymbol{U}_{\boldsymbol{i|2i-1}} + \boldsymbol{Y}^{\boldsymbol{s}}_{\boldsymbol{i|2i-1}}. \tag{45}$$

As noted by Goethals (2005), the primary objective of subspace identification is to extract the extended observability matrix $\boldsymbol{\mathcal{O}}_{\boldsymbol{i}}$ from this equation. The system matrices are obtained in a second step.

Obtaining the observability matrix Starting from the forward innovation description (37-38), one has

$$\boldsymbol{Y}_{\boldsymbol{i|2i-1}} = \boldsymbol{\mathcal{O}}_{\boldsymbol{i}} \hat{\boldsymbol{X}}_{\boldsymbol{i|i}} + \boldsymbol{\mathcal{F}}^{\boldsymbol{d}}_{\boldsymbol{i}} \boldsymbol{U}_{\boldsymbol{i|2i-1}} + \boldsymbol{Y}^{\boldsymbol{f}}_{\boldsymbol{i|2i-1}}, \tag{46}$$

where $\boldsymbol{Y}^{\boldsymbol{f}}_{\boldsymbol{i|2i-1}}$ contains the contributions of the forward innovations:

$$\boldsymbol{Y}^{\boldsymbol{f}}_{\boldsymbol{k_1|k_2}} \triangleq \underbrace{\begin{bmatrix} \boldsymbol{I}_{n_y} & \boldsymbol{0} & \dots & \boldsymbol{0} \\ \boldsymbol{C}_s \boldsymbol{K}^{\boldsymbol{s}}_{\boldsymbol{k_1}} \boldsymbol{S}^{\boldsymbol{r}} & \boldsymbol{I} & \dots & \boldsymbol{0} \\ \vdots & \vdots & \dots & \vdots \\ \boldsymbol{C}_s \boldsymbol{A}_s^{k_2-k_1-1} \boldsymbol{K}^{\boldsymbol{s}}_{\boldsymbol{k_2-1}} \boldsymbol{S}^{\boldsymbol{r}} & \boldsymbol{C}_s \boldsymbol{A}_s^{k_2-k_1-2} \boldsymbol{K}^{\boldsymbol{s}}_{\boldsymbol{k_2-2}} \boldsymbol{S}^{\boldsymbol{r}} & \dots & \boldsymbol{I}_{n_y} \end{bmatrix}}_{\triangleq \boldsymbol{\mathcal{F}}^{\boldsymbol{s}}_{\boldsymbol{k_2-k_1+1}}} \boldsymbol{E}^{\boldsymbol{f}}_{\boldsymbol{k_1|k_2}} \tag{47}$$

and a block Hankel matrix of forward innovations is defined as

$$\boldsymbol{E}^{\boldsymbol{f}}_{\boldsymbol{k_1|k_2}} \triangleq \begin{bmatrix} \boldsymbol{e}^{\boldsymbol{f}}_{\boldsymbol{k_1}} & \boldsymbol{e}^{\boldsymbol{f}}_{\boldsymbol{k_1+1}} & \dots & \boldsymbol{e}^{\boldsymbol{f}}_{\boldsymbol{k_1+j-1}} \\ \boldsymbol{e}^{\boldsymbol{f}}_{\boldsymbol{k_1+1}} & \boldsymbol{e}^{\boldsymbol{f}}_{\boldsymbol{k_1+2}} & \dots & \boldsymbol{e}^{\boldsymbol{f}}_{\boldsymbol{k_1+j}} \\ \vdots & \vdots & \dots & \vdots \\ \boldsymbol{e}^{\boldsymbol{f}}_{\boldsymbol{k_2}} & \boldsymbol{e}^{\boldsymbol{f}}_{\boldsymbol{k_2+1}} & \dots & \boldsymbol{e}^{\boldsymbol{f}}_{\boldsymbol{k_2+j-1}} \end{bmatrix}.$$

$\hat{\boldsymbol{X}}_{\boldsymbol{i|i}}$ contains in each column a non-stationary reference-based Kalman filter state, see Section 2.6, that is estimated from the corresponding columns of $\boldsymbol{U}_{\boldsymbol{0|i-1}}$ and $\boldsymbol{Y}^{\boldsymbol{ref}}_{\boldsymbol{0|i-1}}$. Since the Kalman filter is linear, it follows that $\hat{\boldsymbol{X}}_{\boldsymbol{i|i}}$ lies in the row space of $\boldsymbol{U}_{\boldsymbol{0|i-1}}$, denoted as $\mathscr{U}_{0|i-1}$, and the row space of $\boldsymbol{Y}^{\boldsymbol{ref}}_{\boldsymbol{0|i-1}}$, denoted as $\mathscr{Y}^{ref}_{0|i-1}$. As the row space of $\boldsymbol{U}_{\boldsymbol{0|i-1}}$ is a subset of the row space of $\boldsymbol{U}_{\boldsymbol{0|2i-1}}$, which is denoted as $\mathscr{U}_{0|2i-1}$, one has

$$\text{row space}\left(\hat{\boldsymbol{X}}_{\boldsymbol{i|i}}\right) \subseteq \left(\mathscr{U}_{0|i-1} \vee \mathscr{Y}^{ref}_{0|i-1}\right) \subseteq \left(\mathscr{U}_{0|2i-1} \vee \mathscr{Y}^{ref}_{0|i-1}\right),$$

where $\vee$ denotes joint row space. Given that the forward innovations are uncorrelated with the measured inputs and the outputs that were used for the estimation of the Kalman filter states, projection of both sides of (46) onto the row space spanned by the inputs and the 'past' outputs yields

$$\underset{j\to\infty}{\text{a.s.lim}}\boldsymbol{Y_{i|2i-1}}/\left(\mathscr{U}_{0|2i-1}\vee\mathscr{Y}^{ref}_{0|i-1}\right)=\lim_{j\to\infty}\boldsymbol{\mathcal{O}_i\hat{X}_{i|i}}+\boldsymbol{\mathcal{F}^d_i U_{i|2i-1}}. \tag{48}$$

The *almost-sure limit*, denoted as a.s.lim, is a stochastic limit. A stochastic variable is said to converge almost surely to a certain value, when this convergence holds for almost all realisations of the stochastic variable, except for those with probability zero (Dougherty, 1999). When the orthogonal projection is replaced by an oblique projection along $\mathscr{U}_{i|2i-1}$, the second term of the right hand side drops:

$$\underset{j\to\infty}{\text{a.s.lim}}\boldsymbol{Y_{i|2i-1}}/_{\mathscr{U}_{i|2i-1}}\left(\mathscr{U}_{0|2i-1}\vee\mathscr{Y}^{ref}_{0|i-1}\right)=\lim_{j\to\infty}\boldsymbol{\mathcal{O}_i\hat{X}_{i|i}}.$$

This is the rationale behind the so-called N4SID (*Numerical algorithms for Subspace State Space System IDentification*) approach of Van Overschee and De Moor (1994a). The oblique projection is depicted in Figure 4.

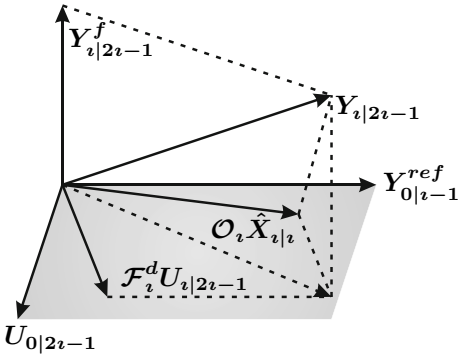

Figure 4. Subspace identification, N4SID approach: graphical representation of the estimation of $\boldsymbol{\mathcal{O}_i\hat{X}_{i|i}}$ from $\boldsymbol{Y_{i|2i-1}}$ by oblique projection.

By introducing left and right weighting matrices $\boldsymbol{W_1}$ and $\boldsymbol{W_2}$,

$$\underset{j\to\infty}{\text{a.s.lim}}\boldsymbol{W_1 Y_{i|2i-1}}/_{\mathscr{U}_{i|2i-1}}\left(\mathscr{U}_{0|2i-1}\vee\mathscr{Y}^{ref}_{0|i-1}\right)\boldsymbol{W_2}=\boldsymbol{W_1}\lim_{j\to\infty}\boldsymbol{\mathcal{O}_i\hat{X}_{i|i}W_2}, \tag{49}$$

it was shown by Van Overschee and De Moor (1994b) that other subspace methods, such as the *Past-Outputs Multi-variable Output-Error State*

sPace (PO-MOESP) method of Verhaegen (1994), and the *Canonical Variate Analysis* (CVA) approach of Larimore (1990), fall into this framework. From a singular value decomposition of the left hand side of this equation, which can be calculated from measured data only, $\boldsymbol{\mathcal{O}_i}$ can be determined up to a nonsingular right factor, after left multiplication with $\boldsymbol{W_1^{-1}}$.

Output-only case. When no inputs are measured, (49) simplifies to the following orthogonal projection:

$$\underset{j\to\infty}{\text{a.s.lim}} \boldsymbol{W_1 Y_{i|2i-1}} / \mathscr{Y}_{0|i-1}^{ref} \boldsymbol{W_2} = \boldsymbol{W_1} \lim_{j\to\infty} \boldsymbol{\mathcal{O}_i \hat{X}_{i|i} W_2}. \tag{50}$$

The projection is graphically depicted in Figure 5. The choice of the weighting matrices is further discussed in Section 4.3.

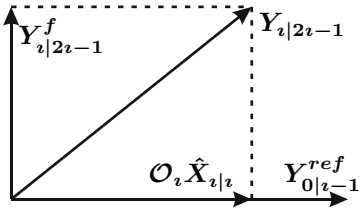

Figure 5. Output-only subspace identification: graphical representation of the estimation of $\boldsymbol{\mathcal{O}_i \hat{X}_{i|i}}$ from $\boldsymbol{Y_{i|2i-1}}$ by orthogonal projection.

4 Subspace identification: algorithms

4.1 Introduction

Three powerful subspace algorithms for the identification of a state-space description from measured data are discussed. In Section 4.2, the *REFerence-based COVariance-driven Stochastic Subspace Identification* (SSI-cov/ref) algorithm is treated. It combines the nonparametric estimation of output correlations with the stochastic realisation algorithm presented in Section 3.2. Advantages of this output-only algorithm are its conceptual simplicity, and the ability to compute the *Probability Density Function* (PDF) of the identified system parameters.

The *REFerence-based DATA-driven Stochastic Subspace Identification* (SSI-data/ref) algorithm is presented in Section 4.3. It is also an output-only system identification algorithm, whose main advantage is an optimal statistical performance when the weighting matrices are properly chosen.

The *REFerence-based DATA-driven Combined deterministic-stochastic Subspace Identification* (CSI-data/ref) algorithm is discussed in Section 4.4. It allows to use exogenous forces in addition to the unmeasured operational excitation. Since these measured forces are exactly known, they reduce the uncertainty of the identified system description compared to the output-only case.

4.2 Covariance-driven stochastic subspace identification

Nonparametric estimation of output correlations. Denote $\boldsymbol{\mathcal{L}^{ref}_{1|2i-1}}$ as the matrix containing stacked stochastic output correlation matrices, i.e.,

$$\boldsymbol{\mathcal{L}^{ref}_{1|2i-1}} \triangleq \begin{bmatrix} \boldsymbol{\Lambda_1^{ref}}^T & \boldsymbol{\Lambda_2^{ref}}^T & \dots & \boldsymbol{\Lambda_{2i-1}^{ref}}^T \end{bmatrix}^T.$$

It can be easily estimated from the measured data:

$$\boldsymbol{\hat{\mathcal{L}}^{ref}_{1|2i-1}} \triangleq \frac{1}{j}\boldsymbol{\hat{Y}_{1|2i-1}}\boldsymbol{\hat{Y}^{ref}_{0|0}}^T.$$

In order to derive the distribution of the correlation estimates, $\boldsymbol{\hat{Y}_{1|2i-1}}$ and $\boldsymbol{\hat{Y}^{ref}_{0|0}}$ are divided into n_B blocks that contain each $j_B = \text{floor}(j/n_B)$ columns, where floor(□) takes the nearest lower integer of the real number □. The blocks are indicated as $\boldsymbol{\hat{Y}_{1|2i-1,k}}$ and $\boldsymbol{\hat{Y}^{ref}_{0|0,k}}$, respectively. If $j = j_B n_B$, one has[2]

$$\boldsymbol{\hat{\mathcal{L}}^{ref}_{1|2i-1}} = \frac{1}{j}\boldsymbol{\hat{Y}^{s}_{1|2i-1}}\boldsymbol{\hat{Y}^{s,ref}_{0|0}}^T = \frac{1}{n_B}\sum_{k=1}^{n_B}\underbrace{\frac{1}{j_B}\boldsymbol{\hat{Y}_{1|2i-1,k}}\boldsymbol{\hat{Y}^{ref}_{0|0,k}}^T}_{\triangleq\boldsymbol{\hat{\mathcal{L}}^{ref}_{1|2i-1,k}}}. \tag{51}$$

When j_B is large enough in order for the $\boldsymbol{\hat{\mathcal{L}}^{ref}_{1|2i-1,k}}$ to be considered as independent samples, the central limit theorem ensures that $\boldsymbol{\hat{\mathcal{L}}^{ref}_{1|2i-1}}$ converges in law to a normal distribution when $n_B \to \infty$. The covariance of $\text{vec}\left(\boldsymbol{\hat{\mathcal{L}}^{ref}_{1|2i-1}}\right)$ can be calculated as the covariance of the sample mean:

$$\boldsymbol{\Sigma}_{\boldsymbol{\hat{\mathcal{L}}^{ref}_{1|2i-1}}} = \frac{1}{n_B(n_B-1)}\sum_{k=1}^{n_B}\text{vec}\left(\Delta\boldsymbol{\hat{\mathcal{L}}^{ref}_{1|2i-1,k}}\right)\text{vec}\left(\Delta\boldsymbol{\hat{\mathcal{L}}^{ref}_{1|2i-1,k}}\right)^T. \tag{52}$$

The operator vec(□) stacks the columns of the matrix □ on top of each other.

[2] If $j \neq j_B n_B$, the last block can contain the additional $j - j_B n_B$ columns. The derivation still holds when this block is scaled with $j_B + (j - j_B n_B)$ instead of j_B.

The SSI-cov/ref algorithm. When the estimate $\hat{\boldsymbol{\mathcal{L}}}_{\mathbf{1|2\imath-1}}^{\boldsymbol{ref}}$, is used to build the block Hankel matrix $\boldsymbol{L}_{\mathbf{1|\imath}}^{\boldsymbol{ref}}$ of the stochastic realisation algorithm presented in Section 3.2, the result makes up an output-only system identification algorithm, called the *(REFerence-based) COVariance-driven Stochastic Subspace Identification* (SSI-cov(/ref)) algorithm[3].

Asymptotic distribution of the estimates. Due to the noise on the measurement data and the fact that only a finite number of samples are available, only approximative estimates $\hat{\boldsymbol{\Lambda}}_{\mathbf{0}}^{\boldsymbol{ref}}$ and $\hat{\boldsymbol{L}}_{\mathbf{1|\imath}}^{\boldsymbol{ref}}$ for the matrices $\boldsymbol{\Lambda}_{\mathbf{0}}^{\boldsymbol{ref}}$ and $\boldsymbol{L}_{\mathbf{1|\imath}}^{\boldsymbol{ref}}$ are available. In addition, the number of nonzero singular values of $\hat{\boldsymbol{L}}_{\mathbf{1|\imath}}^{\boldsymbol{ref}}$ is larger than the system order n, as explained in Section 3.2. Therefore, the realisation algorithm does not yield the exact system matrices $(\boldsymbol{A}, \boldsymbol{G}^{\boldsymbol{ref}}, \boldsymbol{C}, \boldsymbol{\Lambda}_{\mathbf{0}}^{\boldsymbol{ref}}/2)$, but only estimates $(\hat{\boldsymbol{A}}, \hat{\boldsymbol{G}}^{\boldsymbol{ref}}, \hat{\boldsymbol{C}}, \hat{\boldsymbol{\Lambda}}_{\mathbf{0}}^{\boldsymbol{ref}}/2)$. If $\hat{\boldsymbol{L}}_{\mathbf{1|\imath}}^{\boldsymbol{ref}}$ is accurate, its estimation error, defined as

$$\Delta \boldsymbol{L}_{\mathbf{1|\imath}}^{\boldsymbol{ref}} \triangleq \hat{\boldsymbol{L}}_{\mathbf{1|\imath}}^{\boldsymbol{ref}} - \boldsymbol{L}_{\mathbf{1|\imath}}^{\boldsymbol{ref}},$$

is small compared to $\boldsymbol{L}_{\mathbf{1|\imath}}^{\boldsymbol{ref}}$ and $\hat{\boldsymbol{L}}_{\mathbf{1|\imath}}^{\boldsymbol{ref}}$, and the influence of this error on the system realisation $(\hat{\boldsymbol{A}}, \hat{\boldsymbol{G}}^{\boldsymbol{ref}}, \hat{\boldsymbol{C}}, \hat{\boldsymbol{\Lambda}}_{\mathbf{0}}/2)$ can be investigated using a first-order sensitivity analysis, as shown below.

From (39), one has

$$\text{vec}(\boldsymbol{L}_{\mathbf{1|\imath}}) = \boldsymbol{S_1}\text{vec}(\boldsymbol{\mathcal{L}}_{\mathbf{0|2\imath-1}}^{\boldsymbol{ref}}), \qquad \text{vec}(\boldsymbol{\Lambda_0}) = \boldsymbol{S_2}\text{vec}(\boldsymbol{\mathcal{L}}_{\mathbf{0|2\imath-1}}^{\boldsymbol{ref}}), \tag{53}$$

where $\boldsymbol{S_1}$ and $\boldsymbol{S_2}$ are selection matrices,

$$\begin{aligned}
\boldsymbol{S_1} &\triangleq \begin{bmatrix} \boldsymbol{S}_{\mathbf{1,1}}^T & \boldsymbol{S}_{\mathbf{1,2}}^T & \dots & \boldsymbol{S}_{\mathbf{1,\imath}}^T \end{bmatrix}^T \\
\boldsymbol{S_2} &\triangleq \boldsymbol{I}_{n_u} \otimes \begin{bmatrix} \boldsymbol{I}_{n_y} & \boldsymbol{0}_{n_y \times (2\imath-1)n_y} \end{bmatrix} \\
\boldsymbol{S}_{\mathbf{1},k} &\triangleq \boldsymbol{I}_{n_u} \otimes \begin{bmatrix} \boldsymbol{0}_{\imath n_y \times n_y k} & \boldsymbol{I}_{\imath n_y} & \boldsymbol{0}_{\imath n_y \times (\imath-k)n_y} \end{bmatrix},
\end{aligned}$$

and $\otimes$ denotes the Kronecker product.

From (41), a first-order perturbation of $\boldsymbol{\mathcal{O}}_{\boldsymbol{\imath}}$ and $\boldsymbol{\mathcal{C}}_{\boldsymbol{\imath}}^{\boldsymbol{S}}$ can be written as

$$\Delta \boldsymbol{\mathcal{O}}_{\boldsymbol{\imath}} \approx \boldsymbol{U}\frac{1}{2}\boldsymbol{S}^{-1/2}\Delta \boldsymbol{S} + \Delta \boldsymbol{U}\boldsymbol{S}^{1/2} \tag{54}$$

$$\Delta \boldsymbol{\mathcal{C}}_{\boldsymbol{\imath}}^{\boldsymbol{S}} \approx \frac{1}{2}\boldsymbol{S}^{-1/2}\Delta \boldsymbol{S}\boldsymbol{V}^T + \boldsymbol{S}^{1/2}\Delta \boldsymbol{V}^T. \tag{55}$$

[3]Since the stochastic outputs are assumed to have a zero mean value, their correlation matrices equal their covariance matrices, hence the name SSI-*cov*.

The first-order perturbation of $\boldsymbol{S}$ equals (Pintelon et al., 2006):

$$\operatorname{diag}(\Delta \boldsymbol{S}) \approx \begin{bmatrix} (\boldsymbol{v_1} \otimes \boldsymbol{u_1})^T \\ \vdots \\ (\boldsymbol{v_n} \otimes \boldsymbol{u_n})^T \end{bmatrix} \operatorname{vec}(\Delta \boldsymbol{L_{1|\imath}}), \tag{56}$$

where $\operatorname{diag}(\square)$ takes the diagonal of a square matrix $\square$, $\boldsymbol{u_j}$ is the j^{th} column of $\boldsymbol{U}$, and $\boldsymbol{v_j}$ is the j^{th} column of $\boldsymbol{V}$. Pintelon et al. (2006) derived a formula for the first-order sensitivity of the singular vectors of a matrix, which enables one to link $\Delta \boldsymbol{U}$ and $\Delta \boldsymbol{V}$ to $\Delta \boldsymbol{L_{1|\imath}}$:

$$\Delta \boldsymbol{Z} \approx \begin{bmatrix} \boldsymbol{B_1^\dagger C_1} \\ \vdots \\ \boldsymbol{B_n^\dagger C_n} \end{bmatrix} \operatorname{vec}(\Delta \boldsymbol{L_{1|\imath}}), \tag{57}$$

where

$$\begin{aligned} \boldsymbol{Z} &\triangleq \operatorname{vec}\left(\begin{bmatrix} \boldsymbol{U} \\ \boldsymbol{V} \end{bmatrix}\right), \qquad \boldsymbol{C_j} \triangleq \frac{1}{\sigma_j} \begin{bmatrix} \boldsymbol{v_j}^T \otimes (\boldsymbol{I_{\imath n_y}} - \boldsymbol{u_j u_j}^T) \\ \left(\boldsymbol{u_j}^T \otimes (\boldsymbol{I_{\imath n_u}} - \boldsymbol{v_j v_j}^T)\right) \boldsymbol{P_1} \end{bmatrix}, \\ \boldsymbol{B_j} &\triangleq \begin{bmatrix} \boldsymbol{I_{\imath n_y}} & -\frac{\boldsymbol{L_{1|\imath}}}{\sigma_j} \\ -\frac{\boldsymbol{L_{1|\imath}}^T}{\sigma_j} & \boldsymbol{I_{\imath n_u}} \end{bmatrix}, \qquad \boldsymbol{P_1} \triangleq \sum_{k_1=1}^{\imath n_y} \sum_{k_2=1}^{\imath n_u} \boldsymbol{E_{k_1 k_2}^{\imath n_y \times \imath n_u}} \otimes \boldsymbol{E_{k_2 k_1}^{im \times \imath n_y}}. \end{aligned}$$

Using Kronecker algebra (Brewer, 1978) and substituting equations (56-57), (54) yields

$$\begin{aligned} \operatorname{vec}(\Delta \boldsymbol{\mathcal{O}_\imath}) &\approx \left(\boldsymbol{I_n} \otimes \boldsymbol{U} \frac{1}{2} \boldsymbol{S}^{-1/2}\right) \operatorname{vec}(\Delta \boldsymbol{S}) + \left(\boldsymbol{S}^{1/2^T} \otimes \boldsymbol{I_{\imath n_y}}\right) \operatorname{vec}(\Delta \boldsymbol{U}) \\ &\approx (\boldsymbol{\mathcal{A}_1} + \boldsymbol{\mathcal{A}_2}) \operatorname{vec}(\Delta \boldsymbol{L_{1|\imath}}), \end{aligned} \tag{58}$$

where

$$\begin{aligned} \boldsymbol{\mathcal{A}_1} &\triangleq \left(\boldsymbol{I_n} \otimes \left(\frac{1}{2} \boldsymbol{U S}^{-1/2}\right)\right) \boldsymbol{S_3} \begin{bmatrix} (\boldsymbol{v_1} \otimes \boldsymbol{u_1})^T \\ \vdots \\ (\boldsymbol{v_n} \otimes \boldsymbol{u_n})^T \end{bmatrix}, \\ \boldsymbol{\mathcal{A}_2} &\triangleq \underbrace{\left(\boldsymbol{S}^{1/2^T} \otimes \boldsymbol{I_{\imath n_y}}\right) \left(\boldsymbol{I_n} \otimes \begin{bmatrix} \boldsymbol{I_{\imath n_y}} & \boldsymbol{0_{\imath n_y \times \imath n_u}} \end{bmatrix}\right)}_{= \left(\boldsymbol{S}^{1/2^T} \otimes \begin{bmatrix} \boldsymbol{I_{\imath n_y}} & \boldsymbol{0_{\imath n_y \times \imath n_u}} \end{bmatrix}\right)} \begin{bmatrix} \boldsymbol{B_1^\dagger C_1} \\ \vdots \\ \boldsymbol{B_n^\dagger C_n} \end{bmatrix}, \\ \boldsymbol{S_3} &\triangleq \sum_{k=1}^{n} \boldsymbol{E_{(k-1)n+k,k}^{nn \times n}}. \end{aligned}$$

With Kronecker algebra and (56-57), (55) can be converted to

$$\begin{aligned}\mathrm{vec}(\Delta \boldsymbol{\mathcal{C}}_{\boldsymbol{i}}^{\boldsymbol{S}}) &\approx \left(\boldsymbol{V} \otimes \frac{1}{2}\boldsymbol{S}^{-1/2}\right)\Delta \boldsymbol{S} + \left(\boldsymbol{I}_{\imath n_u} \otimes \boldsymbol{S}^{1/2}\right)\boldsymbol{P_2}\mathrm{vec}\Delta \boldsymbol{V} \\ &\approx \boldsymbol{\mathcal{A}_3}\mathrm{vec}(\Delta \boldsymbol{L_{1|\imath}}) + \boldsymbol{\mathcal{A}_4}\mathrm{vec}(\Delta \boldsymbol{L_{1|\imath}}), \end{aligned} \tag{59}$$

where

$$\begin{aligned}\boldsymbol{P_2} &\triangleq \sum_{k_1=1}^{n}\sum_{k_2=1}^{\imath n_u} \boldsymbol{E}^{\imath n_u n \times \imath n_u n}_{\boldsymbol{k_1+(k_2-1)n,(k_1-1)\imath n_u+k_2}} \\ \boldsymbol{\mathcal{A}_3} &\triangleq \left(\boldsymbol{V} \otimes \frac{1}{2}\boldsymbol{S}^{-\frac{1}{2}}\right)\boldsymbol{S_3}\begin{bmatrix}(\boldsymbol{v_1}\otimes\boldsymbol{u_1})^T \\ \vdots \\ (\boldsymbol{v_n}\otimes\boldsymbol{u_n})^T\end{bmatrix} \\ \boldsymbol{\mathcal{A}_4} &\triangleq \left(\boldsymbol{I}_{\imath n_u} \otimes \boldsymbol{S}^{1/2}\right)\boldsymbol{P_2}\left(\boldsymbol{I_n}\otimes\begin{bmatrix}\boldsymbol{0}_{\imath n_u \times \imath n_y} & \boldsymbol{I}_{\imath n_u}\end{bmatrix}\right)\begin{bmatrix}\boldsymbol{B_1^\dagger C_1} \\ \vdots \\ \boldsymbol{B_n^\dagger C_n}\end{bmatrix}.\end{aligned}$$

The first-order perturbation of $\boldsymbol{A}$, calculated via (42), can be expressed as:

$$\mathrm{vec}(\Delta \boldsymbol{A}) \approx \boldsymbol{\mathcal{A}_5}\mathrm{vec}(\Delta \boldsymbol{\mathcal{O}_\imath}),$$

where

$$\begin{aligned}\boldsymbol{\mathcal{A}_5} &\triangleq \boldsymbol{I_n}\otimes(\underline{\boldsymbol{\mathcal{O}_\imath}}^\dagger \boldsymbol{S_4}) - \boldsymbol{A}^T \otimes (\underline{\boldsymbol{\mathcal{O}_\imath}}^\dagger \boldsymbol{S_5}) \\ &\quad + \left((\overline{\boldsymbol{\mathcal{O}_\imath}}^T \boldsymbol{S_5} - \boldsymbol{A}^T \underline{\boldsymbol{\mathcal{O}_\imath}}^T \boldsymbol{S_5}) \otimes (\underline{\boldsymbol{\mathcal{O}_\imath}}^T \underline{\boldsymbol{\mathcal{O}_\imath}})^{-1}\right)\boldsymbol{P_3} \\ \boldsymbol{S_4} &\triangleq \begin{bmatrix}\boldsymbol{0}_{(\imath-1)n_y \times l} & \boldsymbol{I}_{(\imath-1)n_y}\end{bmatrix} \\ \boldsymbol{S_5} &\triangleq \begin{bmatrix}\boldsymbol{I}_{(\imath-1)n_y} & \boldsymbol{0}_{(\imath-1)n_y \times n_y}\end{bmatrix} \\ \boldsymbol{P_3} &\triangleq \sum_{k_1=1}^{n}\sum_{k_2=1}^{\imath n_y} \boldsymbol{E}^{\imath n_y n \times \imath n_y n}_{\boldsymbol{k_1+(k_2-1)n,(k_1-1)\imath n_y+k_2}}.\end{aligned}$$

Substitution of (58) and (53) into this result yields

$$\mathrm{vec}(\Delta \boldsymbol{A}) \approx \boldsymbol{\mathcal{A}_5}\left(\boldsymbol{\mathcal{A}_1}+\boldsymbol{\mathcal{A}_2}\right)\boldsymbol{S_1}\mathrm{vec}(\Delta \boldsymbol{\mathcal{L}^{ref}_{0|2\imath-1}}) = \boldsymbol{\mathcal{A}_6}\mathrm{vec}(\Delta \boldsymbol{\mathcal{L}^{ref}_{0|2\imath-1}}). \tag{60}$$

As $\boldsymbol{G^{ref}}$ corresponds to the first n_r columns of $\boldsymbol{\mathcal{C}_i^S}$, application of (59) and (53) yields

$$\mathrm{vec}(\Delta \boldsymbol{B}) \approx \boldsymbol{\mathcal{A}_7}\left(\boldsymbol{\mathcal{A}_3}+\boldsymbol{\mathcal{A}_4}\right)\boldsymbol{S_1}\mathrm{vec}(\Delta \boldsymbol{\mathcal{L}^{ref}_{0|2\imath-1}}) = \boldsymbol{\mathcal{A}_8}\mathrm{vec}(\Delta \boldsymbol{\mathcal{L}^{ref}_{0|2\imath-1}}), \tag{61}$$

where $\boldsymbol{\mathcal{A}_7} \triangleq \begin{bmatrix} \boldsymbol{I_{nn_u}} & \boldsymbol{0_{n(\imath-1)n_u}} \end{bmatrix}$. As $\boldsymbol{C}$ is determined as the first l rows of $\boldsymbol{\mathcal{O}_\imath}$, application of (58) and (53) leads to

$$\text{vec}(\Delta \boldsymbol{C}) \approx \boldsymbol{\mathcal{A}_9} \left(\boldsymbol{\mathcal{A}_1} + \boldsymbol{\mathcal{A}_2} \right) \boldsymbol{S_1} \text{vec}(\Delta \boldsymbol{\mathcal{L}^{ref}_{0|2\imath-1}}) = \boldsymbol{\mathcal{A}_{10}} \text{vec}(\Delta \boldsymbol{\mathcal{L}^{ref}_{0|2\imath-1}}), \quad (62)$$

where $\boldsymbol{\mathcal{A}_9} = \boldsymbol{I_n} \otimes \begin{bmatrix} \boldsymbol{I_{n_y}} & \boldsymbol{0_{n_y,(\imath-1)n_y}} \end{bmatrix}$. Finally, the application of (53) yields

$$\text{vec}(\Delta \boldsymbol{\Lambda_0}) = \boldsymbol{S_2} \text{vec}(\Delta \boldsymbol{\mathcal{L}^{ref}_{0|2\imath-1}}). \quad (63)$$

With the definition

$$\boldsymbol{\mathcal{A}} \triangleq \begin{bmatrix} \boldsymbol{\mathcal{A}_6^T} & \boldsymbol{\mathcal{A}_8^T} & \boldsymbol{\mathcal{A}_{10}^T} & \boldsymbol{S_2^T} \end{bmatrix}^T,$$

the following expression for the covariances of the identified system matrices is obtained (Reynders et al., 2008):

$$\boldsymbol{\Sigma}_{\hat{\boldsymbol{A}}, \hat{\boldsymbol{G}}^{\boldsymbol{ref}}, \hat{\boldsymbol{C}}, \hat{\boldsymbol{\Lambda}}_{\boldsymbol{0}}^{\boldsymbol{ref}}/\boldsymbol{2}} = \boldsymbol{\mathcal{A}} \boldsymbol{\Sigma}_{\boldsymbol{\hat{\mathcal{L}}^{ref}_{0|2\imath-1}}} \boldsymbol{\mathcal{A}}^T, \qquad \Delta \boldsymbol{\mathcal{L}^{ref}_{0|2\imath-1}} \to \boldsymbol{0}, \quad (64)$$

where

$$\boldsymbol{\Sigma}_{\hat{\boldsymbol{A}}, \hat{\boldsymbol{G}}^{\boldsymbol{ref}}, \hat{\boldsymbol{C}}, \hat{\boldsymbol{\Lambda}}_{\boldsymbol{0}}^{\boldsymbol{ref}}/\boldsymbol{2}} \triangleq \text{Cov}\left(\begin{bmatrix} \text{vec}(\hat{\boldsymbol{A}})^T & \text{vec}(\hat{\boldsymbol{G}}^{\boldsymbol{ref}})^T & \text{vec}(\hat{\boldsymbol{C}})^T & \text{vec}(\hat{\boldsymbol{\Lambda}}_{\boldsymbol{0}}^{\boldsymbol{ref}})^T \end{bmatrix}^T \right).$$

Since the output correlations are asymptotically normally distributed, it follows from the first-order sensitivity analysis that the same holds for the estimated system matrices, when $\Delta \boldsymbol{\mathcal{L}^{ref}_{0|2\imath-1}} \to \boldsymbol{0}$.

A note on the choice of $\imath$. In theory, any value $\imath$ that is larger than $\text{ceil}(n/n_y) + 1$ with $\text{ceil}(\square)$ a function that rounds real argument $\square$ to the nearest integer towards $+\infty$, can be chosen for the identification. However, the quality of the identified system model depends on this choice. If the lowest eigenfrequency f_1 of the structure is low compared to the sampling frequency, and if the value of $\imath$ is low, it is possible that each column of $\boldsymbol{H_{1|\imath}}$ contains only a small part of the corresponding eigenperiod and as a consequence the eigenfrequency is not well identified. A solution is to choose $\imath$ as large as possible, but then the calculation time and memory usage might become excessive. Therefore, Reynders and De Roeck (2008) proposed the following rule of thumb for choosing $\imath$:

$$\imath \geq \frac{1}{2 f_0 T}, \quad (65)$$

with f_0 the lowest frequency of interest.

Summary. Figure 6 lists the different steps of the SSI-cov/ref algorithm for the identification of the state-space matrices $\boldsymbol{A}$, $\boldsymbol{G^{ref}}$, $\boldsymbol{C}$, and $\boldsymbol{\Lambda_0}$ and the estimation of their joint probability density function.

SSI-cov/ref algorithm.

1. Compute $\hat{\boldsymbol{\mathcal{L}}}^{\boldsymbol{ref}}_{\boldsymbol{1|2i-1}}$ and $\boldsymbol{\Sigma}_{\hat{\boldsymbol{\mathcal{L}}}^{\boldsymbol{ref}}_{\boldsymbol{1|2i-1}}}$ using (51) and (52), respectively. Build $\boldsymbol{L}^{\boldsymbol{ref}}_{\boldsymbol{1|i}}$ using (39).
2. Choose the system order n and compute the extended observability matrix $\boldsymbol{\mathcal{O}_i}$ and the reference-based extended stochastic controllability matrix $\boldsymbol{\mathcal{C}^S_i}$ from the singular value decomposition of $\boldsymbol{L}^{\boldsymbol{ref}}_{\boldsymbol{1|i}}$ using (41).
3. Estimate the state-space matrices. $\hat{\boldsymbol{C}}$ equals the first n_y rows of $\boldsymbol{\mathcal{O}_i}$, $\hat{\boldsymbol{G}}^{\boldsymbol{ref}}$ equals the first n_r columns of $\boldsymbol{\mathcal{C}_i}$, and $\hat{\boldsymbol{A}}$ is determined from (42).
4. Compute $\boldsymbol{\Sigma}_{\hat{\boldsymbol{A}},\hat{\boldsymbol{G}}^{\boldsymbol{ref}},\hat{\boldsymbol{C}},\hat{\boldsymbol{\Lambda}}^{\boldsymbol{ref}}_{\boldsymbol{0}}/\boldsymbol{2}}$ using (64), where an expression for $\boldsymbol{\mathcal{A}}$ is derived in the above linear sensitivity analysis.

Figure 6. The SSI-cov/ref algorithm with estimation of the probability density function of the estimated state-space matrices.

4.3 Data-driven stochastic subspace identification

A strongly consistent subspace algorithm. In Section 3.3, it was derived that, under assumption 3.1,

$$\underset{j\to\infty}{\text{a.s.lim}}\boldsymbol{W_1}\boldsymbol{Y^s_{i|2i-1}}/\mathscr{Y}^{s,ref}_{0|i-1}\boldsymbol{W_2} = \boldsymbol{W_1}\lim_{j\to\infty}\boldsymbol{\mathcal{O}_i}\hat{\boldsymbol{X}}_{\boldsymbol{i|i}}\boldsymbol{W_2}. \tag{50}$$

This is the basic relationship for the *DATA-driven Stochastic Subspace Identification* (SSI-data) class of subspace algorithms, that only differ up to specific choices for the weighting matrices $\boldsymbol{W_1}$ and $\boldsymbol{W_2}$. From the reduced singular value decomposition

$$\boldsymbol{W_1}\boldsymbol{Y^s_{i|2i-1}}/\mathscr{Y}^{s,ref}_{0|i-1}\boldsymbol{W_2} \approx \boldsymbol{USV}^T,$$

where the diagonal matrix $\boldsymbol{S} \in \mathbb{R}^{n\times n}$ contains only the n highest singular values and $\boldsymbol{U} \in \mathbb{R}^{in_y\times n}$ and $\boldsymbol{V} \in \mathbb{R}^{j\times n}$ contain the corresponding singular vectors, it follows from (50) that the following estimates are strongly

consistent[4] under assumption 3.1:

$$\hat{\boldsymbol{\mathcal{O}}}_{\boldsymbol{\imath}} \triangleq \boldsymbol{W_1^{-1}} \boldsymbol{U} \boldsymbol{S}^{\frac{1}{2}}, \qquad \hat{\hat{\boldsymbol{X}}}^{\boldsymbol{s}}_{\boldsymbol{\imath}|\boldsymbol{\imath}} \triangleq \hat{\boldsymbol{\mathcal{O}}}_{\boldsymbol{\imath}}^{\dagger} \boldsymbol{Y}^{\boldsymbol{s}}_{\boldsymbol{\imath}|\boldsymbol{2\imath}-\boldsymbol{1}} / \mathscr{Y}^{s,ref}_{0|\imath-1}, \qquad \text{and}$$
$$\hat{\hat{\boldsymbol{X}}}^{\boldsymbol{s}}_{\boldsymbol{\imath}+\boldsymbol{1}|\boldsymbol{\imath}+\boldsymbol{1}} \triangleq \underline{\hat{\boldsymbol{\mathcal{O}}}_{\boldsymbol{\imath}}}^{\dagger} \boldsymbol{Y}^{\boldsymbol{s}}_{\boldsymbol{\imath}+\boldsymbol{1}|\boldsymbol{2\imath}-\boldsymbol{1}} / \mathscr{Y}^{s,ref}_{0|\imath}. \tag{66}$$

From the reference-based forward innovation model (37-38), one has

$$\begin{bmatrix} \hat{\boldsymbol{X}}^{\boldsymbol{s}}_{\boldsymbol{\imath}+\boldsymbol{1}|\boldsymbol{\imath}+\boldsymbol{1}} \\ \boldsymbol{Y}_{\boldsymbol{\imath}|\boldsymbol{\imath}} \end{bmatrix} = \begin{bmatrix} \boldsymbol{A} \\ \boldsymbol{C} \end{bmatrix} \hat{\boldsymbol{X}}^{\boldsymbol{s}}_{\boldsymbol{\imath}|\boldsymbol{\imath}} + \begin{bmatrix} \boldsymbol{K}_{\boldsymbol{\imath}} \boldsymbol{E}^{\boldsymbol{f,ref}}_{\boldsymbol{\imath}|\boldsymbol{\imath}} \\ \boldsymbol{E}^{\boldsymbol{f}}_{\boldsymbol{\imath}|\boldsymbol{\imath}} \end{bmatrix}. \tag{67}$$

Since it can be shown that $\mathcal{E}\left(\boldsymbol{e_k} \hat{\boldsymbol{x}}^{\boldsymbol{s}\,T}_{\boldsymbol{k}}\right) = \boldsymbol{0}$, one has

$$\underset{\jmath\to\infty}{\text{a.s.lim}} \begin{bmatrix} \hat{\boldsymbol{X}}^{\boldsymbol{s}}_{\boldsymbol{\imath}+\boldsymbol{1}|\boldsymbol{\imath}+\boldsymbol{1}} \\ \boldsymbol{Y}_{\boldsymbol{\imath}|\boldsymbol{\imath}} \end{bmatrix} \hat{\boldsymbol{X}}^{\boldsymbol{s}\,\dagger}_{\boldsymbol{\imath}|\boldsymbol{\imath}} = \begin{bmatrix} \boldsymbol{A} \\ \boldsymbol{C} \end{bmatrix},$$

so an estimate of $\boldsymbol{A}$ and $\boldsymbol{C}$ that is strongly consistent under assumption 3.1 is obtained from

$$\begin{bmatrix} \hat{\boldsymbol{A}} \\ \hat{\boldsymbol{C}} \end{bmatrix} \triangleq \begin{bmatrix} \hat{\hat{\boldsymbol{X}}}^{\boldsymbol{s}}_{\boldsymbol{\imath}+\boldsymbol{1}|\boldsymbol{\imath}+\boldsymbol{1}} \\ \boldsymbol{Y}_{\boldsymbol{\imath}|\boldsymbol{\imath}} \end{bmatrix} \hat{\hat{\boldsymbol{X}}}^{\boldsymbol{s}\,\dagger}_{\boldsymbol{\imath}|\boldsymbol{\imath}}. \tag{68}$$

As explained in Section 2.6, $\boldsymbol{K_\imath} \to \boldsymbol{K}$ when $\imath \to \infty$. Therefore, one has

$$\underset{\imath,\jmath\to\infty}{\text{a.s.lim}} \frac{1}{\jmath} \begin{bmatrix} \boldsymbol{K}_{\boldsymbol{\imath}} \boldsymbol{E}^{\boldsymbol{f,ref}}_{\boldsymbol{\imath}|\boldsymbol{\imath}} \\ \boldsymbol{E}^{\boldsymbol{f}}_{\boldsymbol{\imath}|\boldsymbol{\imath}} \end{bmatrix} \begin{bmatrix} \boldsymbol{K}_{\boldsymbol{\imath}} \boldsymbol{E}^{\boldsymbol{f,ref}}_{\boldsymbol{\imath}|\boldsymbol{\imath}} \\ \boldsymbol{E}^{\boldsymbol{f}}_{\boldsymbol{\imath}|\boldsymbol{\imath}} \end{bmatrix}^T = \begin{bmatrix} \boldsymbol{Q^{ref}} & \boldsymbol{S^{ref}} \\ \boldsymbol{S^{ref}}^T & \boldsymbol{R} \end{bmatrix}.$$

For finite $\imath$ and $\jmath$, the left-hand side of this equation can be estimated from (67), after estimating $\boldsymbol{A}$ and $\boldsymbol{C}$. From the equations (29), (30), (31), (34), and (35), it is then possible to calculate estimates for $\boldsymbol{\Sigma^s}$, $\boldsymbol{G}$, $\boldsymbol{\Lambda_0}$, $\boldsymbol{K}$, and $\boldsymbol{P}$, respectively.

Asymptotic statistical efficiency and the choice of weighting matrices. The general formulation of the SSI-data/ref algorithm presented above leaves some freedom in the choice of the weighting matrices $\boldsymbol{W_1}$ and $\boldsymbol{W_2}$. In order not to lose the consistency property, it is obvious that $\boldsymbol{W_1}$ should be of full rank, and that $\boldsymbol{W_2}$ should preserve the rank of the matrices with which it is multiplied. Van Overschee and De Moor (1996) showed that by specific choices of the weighting matrices, the SSI-cov/ref algorithm,

[4] An estimate is strongly consistent when its almost-sure limit equals the exact value.

presented in Section 4.2, the *Unweighted Principal Component* (UPC) algorithm of Arun and Kung (1990), and the CVA approach (Akaike, 1974, 1975; Arun and Kung, 1990) fit into this framework.

For a correctly specified system order n, the choice of the weighting matrix $\boldsymbol{W_2}$ doesn't have an influence on the asymptotic distribution of the estimated system, see Bauer et al. (2000), but as shown by Bauer and Ljung (2002), the choice of $\boldsymbol{W_1}$ is important. Recently, Bauer (2005) proved that the output-only CVA algorithm, for which

$$\boldsymbol{W_1} = \left(\frac{1}{\jmath}\boldsymbol{Y_{\imath|2\imath-1}}\boldsymbol{Y_{\imath|2\imath-1}^T}\right)^{-1/2} \qquad \text{and} \qquad \boldsymbol{W_2} = \boldsymbol{I_\jmath},$$

is asymptotically statistically efficient for $\jmath \to \infty$. This means that the covariance matrix of the estimates equals asymptotically the Cramér-Rao lower bound, i.e., no estimator with lower covariance can be found. Since the choice of $\boldsymbol{W_2}$ is unimportant, this result obviously holds for a class of algorithms having the same $\boldsymbol{W_1}$ as CVA, called the *Larimore type* of algorithms. This type of algorithms leads to a theoretically optimal choice of weighting matrices. Also for SSI-data/ref, the rule of thumb (65) for the choice of $\imath$ is advised.

Implementation. As shown by Peeters and De Roeck (1999), the SSI-data/ref algorithm can be efficiently implemented by making use of the LQ-factorisation technique, where the explicit computation of the Q factor can be avoided. Figure 7 contains a step-by-step overview of this implementation in case of CVA weighting.

4.4 Data-driven combined deterministic-stochastic subspace identification

Introduction. The *REFerence-based DATA-driven Combined Subspace Identification* (CSI-data/ref) algorithm of Reynders and De Roeck (2008) identifies the combined deterministic-stochastic state-space model that was presented in Section 2.6. It is the reference-based generalisation of the robust combined subspace algorithm of Van Overschee and De Moor (1996).

A strongly consistent subspace algorithm. In Section 3.3, it was derived that, under assumptions 3.1, 3.2, and 3.3,

$$\underset{\jmath\to\infty}{\text{a.s.lim}}\boldsymbol{W_1}\boldsymbol{Y_{\imath|2\imath-1}}/\mathscr{U}_{\imath|2\imath-1}\left(\mathscr{U}_{0|2\imath-1} \vee \mathscr{Y}^{ref}_{0|\imath-1}\right)\boldsymbol{W_2} = \boldsymbol{W_1} lim_{\jmath\to\infty}\boldsymbol{\mathcal{O}_\imath}\boldsymbol{\hat{X}_{\imath|\imath}}\boldsymbol{W_2}. \quad (49)$$

This is the basic relationship for the CSI-data/ref class of algorithms, that only differ up to the weighting matrices $\boldsymbol{W_1}$ and $\boldsymbol{W_2}$. The initial-

SSI-data/ref algorithm (CVA weighting).

1. Construct the block Hankel matrices $\boldsymbol{Y}_{0|\imath}^{s,ref}$, $\boldsymbol{Y}_{\imath+1|2\imath-1}^{s}$, and $\boldsymbol{Y}_{\imath|\imath}^{s,\ ref}$, where $\boldsymbol{Y}_{\imath|\imath}^{s,\tilde{}ref}$ contains the non-reference rows of $\boldsymbol{Y}_{\imath|\imath}^{s}$. Perform the following LQ decomposition, with $\boldsymbol{L}$ lower triangular and $\boldsymbol{Q}$ orthonormal:

$$\begin{bmatrix} \boldsymbol{Y}_{0|\imath-1}^{s,ref} \\ \boldsymbol{Y}_{\imath|\imath}^{s,ref} \\ \boldsymbol{Y}_{\imath|\imath}^{s,\tilde{}ref} \\ \boldsymbol{Y}_{\imath+1|2\imath-1}^{s} \end{bmatrix} = \frac{1}{\sqrt{j}} \underbrace{\begin{bmatrix} \boldsymbol{L_{11}} & \boldsymbol{0} & \boldsymbol{0} & \boldsymbol{0} \\ \boldsymbol{L_{21}} & \boldsymbol{L_{22}} & \boldsymbol{0} & \boldsymbol{0} \\ \boldsymbol{L_{31}} & \boldsymbol{L_{32}} & \boldsymbol{L_{33}} & \boldsymbol{0} \\ \boldsymbol{L_{41}} & \boldsymbol{L_{42}} & \boldsymbol{L_{43}} & \boldsymbol{L_{44}} \end{bmatrix}}_{\boldsymbol{L}} \underbrace{\begin{bmatrix} \boldsymbol{Q_1} \\ \boldsymbol{Q_2} \\ \boldsymbol{Q_3} \\ \boldsymbol{Q_4} \end{bmatrix}}_{\boldsymbol{Q}},$$

   where $\boldsymbol{L_{11}} \in \mathbb{R}^{\imath n_r \times \imath n_r}$, $\boldsymbol{L_{22}} \in \mathbb{R}^{n_r \times n_r}$, and $\boldsymbol{L_{33}} \in \mathbb{R}^{(n_y-n_r)\times(n_y-n_r)}$. $\boldsymbol{Q}$ does not need to be determined.
2. Compute $\boldsymbol{W_1}$ as

$$\boldsymbol{W_1} = \begin{bmatrix} \boldsymbol{L_{21}} & \boldsymbol{L_{22}} & \boldsymbol{0} & \boldsymbol{0} \\ \boldsymbol{L_{31}} & \boldsymbol{L_{32}} & \boldsymbol{L_{33}} & \boldsymbol{0} \\ \boldsymbol{L_{41}} & \boldsymbol{L_{42}} & \boldsymbol{L_{43}} & \boldsymbol{L_{44}} \end{bmatrix} \begin{bmatrix} \boldsymbol{L_{21}} & \boldsymbol{L_{22}} & \boldsymbol{0} & \boldsymbol{0} \\ \boldsymbol{L_{31}} & \boldsymbol{L_{32}} & \boldsymbol{L_{33}} & \boldsymbol{0} \\ \boldsymbol{L_{41}} & \boldsymbol{L_{42}} & \boldsymbol{L_{43}} & \boldsymbol{L_{44}} \end{bmatrix}^T.$$

3. Compute the singular value decomposition $\boldsymbol{USV}^T = \boldsymbol{W_1} \begin{bmatrix} \boldsymbol{L_{21}} \\ \boldsymbol{L_{31}} \\ \boldsymbol{L_{41}} \end{bmatrix}$. Choose the system order n and retain only the n highest singular values and the corresponding singular vectors.
4. Compute the observability matrix as $\hat{\boldsymbol{\mathcal{O}}}_{\imath} = \boldsymbol{W_1}^{-1}\boldsymbol{US}^{\frac{1}{2}}$. Determine $\underline{\boldsymbol{\mathcal{O}_{\imath}}}$ by deleting the last n_y rows of $\hat{\boldsymbol{\mathcal{O}}}_{\imath}$.
5. Finally, compute the system estimates:

$$\begin{bmatrix} \hat{\boldsymbol{A}} \\ \hat{\boldsymbol{C}} \end{bmatrix} = \begin{bmatrix} \underline{\boldsymbol{\mathcal{O}_{\imath}}}^{\dagger}\boldsymbol{L_{41}} \\ \boldsymbol{L_{21}} \\ \boldsymbol{L_{31}} \end{bmatrix} \left(\hat{\boldsymbol{\mathcal{O}}}_{\imath}^{\dagger} \begin{bmatrix} \boldsymbol{L_{21}} \\ \boldsymbol{L_{31}} \\ \boldsymbol{L_{41}} \end{bmatrix} \right)^{\dagger}.$$

Figure 7. Implementation of the SSI-data/ref CVA algorithm.

state matrix for the sequence of reference-based Kalman filter states $\hat{\boldsymbol{X}}_{\boldsymbol{i|i}}$ is $\hat{\boldsymbol{X}}_{\boldsymbol{0|0}} = \hat{\boldsymbol{X}}^{\boldsymbol{d}}_{\boldsymbol{0|0}} / \mathscr{U}_{i|2i-1} \mathscr{U}_{0|i-1}$. Using the reduced singular value decomposition

$$\boldsymbol{W_1 Y_{i|2i-1}} / \mathscr{U}_{i|2i-1} \left(\mathscr{U}_{0|2i-1} \vee \mathscr{Y}^{ref}_{0|i-1} \right) \boldsymbol{W_2} \approx \boldsymbol{U S V}^T,$$

where the diagonal matrix $\boldsymbol{S} \in \mathbb{R}^{n \times n}$ contains the highest n singular values and $\boldsymbol{U} \in \mathbb{R}^{i(n_y+n_u) \times n}$ and $\boldsymbol{V} \in \mathbb{R}^{j \times n}$ contain the corresponding singular vectors, one has from (49) that the following estimate for the observability matrix is strongly consistent under assumptions 3.1, 3.2, and 3.3:

$$\hat{\boldsymbol{\mathcal{O}}}_{\boldsymbol{i}} \triangleq \boldsymbol{W_1^{-1} U S^{\frac{1}{2}}}. \tag{69}$$

For the estimation of $\hat{\boldsymbol{X}}_{\boldsymbol{i|i}}$ and $\hat{\boldsymbol{X}}_{\boldsymbol{i+1|i+1}}$, (49) can unfortunately not be used since the initial state matrix of $\hat{\boldsymbol{X}}_{\boldsymbol{i+1|i+1}}$ would be $\hat{\boldsymbol{X}}^{\boldsymbol{d}}_{\boldsymbol{0|0}} / \mathscr{U}_{i+1|2i} \mathscr{U}_{0|i}$, which is different from the initial state matrix of $\hat{\boldsymbol{X}}_{\boldsymbol{i|i}}$. As noted in Van Overschee and De Moor (1994a), this would lead to an inconsistent algorithm for finite values of i. Therefore, the orthogonal projection (48), which was derived in Section 3.3, is considered instead:

$$\operatorname*{a.s.lim}_{j \to \infty} \underbrace{\boldsymbol{Y_{i|2i-1}} / \left(\mathscr{U}_{0|2i-1} \vee \mathscr{Y}^{ref}_{0|i-1} \right)}_{\triangleq \boldsymbol{\mathcal{Z}_i}} = \lim_{j \to \infty} \boldsymbol{\mathcal{O}_i \hat{X}_{i|i}} + \boldsymbol{\mathcal{F}^d_i U_{i|2i-1}}. \tag{48}$$

The initial state matrix for the sequence of reference-based Kalman filter states $\hat{\boldsymbol{X}}_{\boldsymbol{i|i}}$ is now $\hat{\boldsymbol{X}}_{\boldsymbol{0|0}} = \hat{\boldsymbol{X}}^{\boldsymbol{d}}_{\boldsymbol{0|0}} / \mathscr{U}_{0|2i-1}$. Following the same lines, one has

$$\begin{aligned} \operatorname*{a.s.lim}_{j \to \infty} & \underbrace{\boldsymbol{Y_{i+1|2i-1}} / \left(\mathscr{U}_{0|2i-1} \vee \mathscr{Y}^{ref}_{0|i} \right)}_{\triangleq \boldsymbol{\mathcal{Z}_{i+1}}} \\ & = \lim_{j \to \infty} \boldsymbol{\mathcal{O}_{i-1} \hat{X}_{i+1|i+1}} + \boldsymbol{\mathcal{F}^d_{i-1} U_{i+1|2i-1}}, \end{aligned} \tag{70}$$

where $\hat{\boldsymbol{X}}_{\boldsymbol{i+1|i+1}}$ has the same initial state matrix as in the previous expression. From the reference-based forward innovation model (37-38), one has

$$\begin{bmatrix} \hat{\boldsymbol{X}}_{\boldsymbol{i+1|i+1}} \\ \boldsymbol{Y_{i|i}} \end{bmatrix} = \begin{bmatrix} \boldsymbol{A} \\ \boldsymbol{C} \end{bmatrix} \hat{\boldsymbol{X}}_{\boldsymbol{i|i}} + \begin{bmatrix} \boldsymbol{B} \\ \boldsymbol{D} \end{bmatrix} \boldsymbol{U_{i|i}} + \begin{bmatrix} \boldsymbol{K_i E^{f,ref}_{i|i}} \\ \boldsymbol{E^f_{i|i}} \end{bmatrix}. \tag{71}$$

Substitution of (69-70) yields

$$\operatorname*{a.s.lim}_{j \to \infty} \left[\hat{\boldsymbol{\mathcal{O}}}^{\dagger}_{\boldsymbol{i-1}} \boldsymbol{\mathcal{Z}_{i+1}} \right] = \lim_{j \to \infty} \begin{bmatrix} \boldsymbol{A} \\ \boldsymbol{C} \end{bmatrix} \hat{\boldsymbol{\mathcal{O}}}^{\dagger}_{\boldsymbol{i}} \boldsymbol{\mathcal{Z}_i} + \boldsymbol{K_i U_{i|2i-1}} + \begin{bmatrix} \boldsymbol{K_i E^{f,ref}_{i|i}} \\ \boldsymbol{E^f_{i|i}} \end{bmatrix}, \tag{72}$$

where

$$\boldsymbol{K}_{\boldsymbol{\imath}} = \begin{bmatrix} -\boldsymbol{A}\boldsymbol{\mathcal{O}}_{\boldsymbol{\imath}}^{\dagger}\boldsymbol{\mathcal{F}}_{\boldsymbol{\imath}}^{\boldsymbol{d}} + \begin{bmatrix} \boldsymbol{B} & \boldsymbol{\mathcal{O}}_{\boldsymbol{\imath-1}}^{\dagger}\boldsymbol{\mathcal{F}}_{\boldsymbol{\imath-1}}^{\boldsymbol{d}} \end{bmatrix} \\ -\boldsymbol{C}\boldsymbol{\mathcal{O}}_{\boldsymbol{\imath}}^{\dagger}\boldsymbol{\mathcal{F}}_{\boldsymbol{\imath}}^{\boldsymbol{d}} + \begin{bmatrix} \boldsymbol{D} & \boldsymbol{0} \end{bmatrix} \end{bmatrix}. \tag{73}$$

Since the state estimation error $\boldsymbol{e_k}$ is orthogonal to the state estimate $\hat{\boldsymbol{x}}_{\boldsymbol{k}}$ (Juang, 1994), it follows that a strongly consistent estimate of $\boldsymbol{A}$, $\boldsymbol{C}$, and $\boldsymbol{K}_{\boldsymbol{\imath}}$ is obtained from

$$\begin{bmatrix} \begin{bmatrix} \hat{\boldsymbol{A}} \\ \hat{\boldsymbol{C}} \end{bmatrix} & \hat{\boldsymbol{K}}_{\boldsymbol{\imath}} \end{bmatrix} \triangleq \begin{bmatrix} \hat{\boldsymbol{\mathcal{O}}}_{\boldsymbol{\imath-1}}^{\dagger}\boldsymbol{Y}_{\boldsymbol{\imath+1|2\imath}} / \left(\mathscr{U}_{0|2\imath-1} \vee \mathscr{Y}_{0|\imath}^{ref} \right) \\ \boldsymbol{Y}_{\boldsymbol{\imath|\imath}} \end{bmatrix} \begin{bmatrix} \hat{\boldsymbol{\mathcal{O}}}_{\boldsymbol{\imath}}^{\dagger}\boldsymbol{Y}_{\boldsymbol{\imath|2\imath-1}} / \left(\mathscr{U}_{0|2\imath-1} \vee \mathscr{Y}_{0|\imath-1}^{ref} \right) \\ \boldsymbol{U}_{\boldsymbol{\imath|\imath}} \end{bmatrix}^{\dagger}.$$

$\boldsymbol{K}_{\boldsymbol{\imath}}$ is linear in $\boldsymbol{B}$ and $\boldsymbol{D}$ (see (73)), so if $\boldsymbol{K}_{\boldsymbol{\imath,k}} \in \mathbb{R}^{n \times n_u}$ is defined as the k^{th} block column of $\boldsymbol{K}_{\boldsymbol{\imath}}$, $\boldsymbol{\mathcal{M}_k} \in \mathbb{R}^{n \times n_y}$ as the k^{th} block column of $\boldsymbol{\mathcal{O}}_{\boldsymbol{\imath-1}}^{\dagger}$, $\boldsymbol{\mathcal{L}_{1,k}} \in \mathbb{R}^{n \times n_y}$ as the k^{th} block column of $\boldsymbol{A}\boldsymbol{\mathcal{O}}_{\boldsymbol{\imath}}^{\dagger}$ and $\boldsymbol{\mathcal{L}_{2,k}} \in \mathbb{R}^{n_y \times n_y}$ as the k^{th} block column of $\boldsymbol{C}\boldsymbol{\mathcal{O}}_{\boldsymbol{\imath}}^{\dagger}$, one has:

$$\begin{aligned} \boldsymbol{K}_{\boldsymbol{\imath,k}} &= \boldsymbol{\mathcal{N}_k} \begin{bmatrix} \boldsymbol{D}^T & \boldsymbol{B}^T \end{bmatrix}^T \\ \boldsymbol{\mathcal{N}_1} &= \begin{bmatrix} -\boldsymbol{\mathcal{L}_{11}} & \boldsymbol{\mathcal{M}_1} - \boldsymbol{\mathcal{L}_{12}} & \cdots & \boldsymbol{\mathcal{M}_{\imath-1}} - \boldsymbol{\mathcal{L}_{1\imath}} \\ \boldsymbol{I_{n_y}} - \boldsymbol{\mathcal{L}_{21}} & -\boldsymbol{\mathcal{L}_{22}} & \cdots & -\boldsymbol{\mathcal{L}_{2\imath}} \end{bmatrix} \begin{bmatrix} \boldsymbol{I_{n_y}} & \boldsymbol{0} \\ \boldsymbol{0} & \boldsymbol{\mathcal{O}_i} \end{bmatrix} \\ \boldsymbol{\mathcal{N}_{k \neq 1}} &= \begin{bmatrix} \boldsymbol{\mathcal{M}_{k-1}} - \boldsymbol{\mathcal{L}_{1k}} & \cdots & \boldsymbol{\mathcal{M}_{\imath-1}} - \boldsymbol{\mathcal{L}_{1\imath}} & \boldsymbol{0_{n \times l(k-1)}} \\ -\boldsymbol{\mathcal{L}_{2k}} & \cdots & -\boldsymbol{\mathcal{L}_{2\imath}} & \boldsymbol{0_{l \times l(k-1)}} \end{bmatrix} \begin{bmatrix} \boldsymbol{I_{n_y}} & \boldsymbol{0} \\ \boldsymbol{0} & \boldsymbol{\mathcal{O}_i} \end{bmatrix}. \end{aligned}$$

With this factorisation, it follows from (72) that strongly consistent estimates of $\boldsymbol{B}$ and $\boldsymbol{D}$ can be obtained from

$$\operatorname{vec}\left(\begin{bmatrix} \hat{\boldsymbol{D}} \\ \hat{\boldsymbol{B}} \end{bmatrix} \right) = \left(\sum_{k=1}^{\imath+1} \boldsymbol{U}_{\boldsymbol{\imath+k-1|\imath+k-1}}^{T} \otimes \hat{\boldsymbol{\mathcal{N}}}_{\boldsymbol{k}} \right)^{\dagger} \operatorname{vec}(\hat{\boldsymbol{\mathcal{P}}})$$

$$\hat{\boldsymbol{\mathcal{P}}} \triangleq \begin{bmatrix} \hat{\boldsymbol{\mathcal{O}}}_{\boldsymbol{\imath-1}}^{\dagger}\boldsymbol{\mathcal{Z}}_{\boldsymbol{\imath+1}} \\ \boldsymbol{Y}_{\boldsymbol{\imath}} \end{bmatrix} - \begin{bmatrix} \hat{\boldsymbol{A}} \\ \hat{\boldsymbol{C}} \end{bmatrix} \boldsymbol{\mathcal{O}}_{\boldsymbol{\imath}}^{\dagger}\boldsymbol{\mathcal{Z}}_{\boldsymbol{\imath}},$$

where $\boldsymbol{U}_{\boldsymbol{\imath+k-1|\imath+k-1}}$ is the $(\imath + k - 1)^{\text{th}}$ block row of $\boldsymbol{U}_{\boldsymbol{0|2\imath-1}}$. Finally, the noise covariance matrices can be estimated from the residuals of (71):

$$\underset{\imath,\jmath \to \infty}{\text{a.s.lim}} \frac{1}{\jmath} \begin{bmatrix} \boldsymbol{K}_{\boldsymbol{\imath}} \boldsymbol{E}_{\boldsymbol{\imath|\imath}}^{\boldsymbol{f,ref}} \\ \boldsymbol{E}_{\boldsymbol{\imath|\imath}}^{\boldsymbol{f}} \end{bmatrix} \begin{bmatrix} \boldsymbol{K}_{\boldsymbol{\imath}} \boldsymbol{E}_{\boldsymbol{\imath|\imath}}^{\boldsymbol{f,ref}} \\ \boldsymbol{E}_{\boldsymbol{\imath|\imath}}^{\boldsymbol{f}} \end{bmatrix}^{T} = \begin{bmatrix} \boldsymbol{Q} & \boldsymbol{S} \\ \boldsymbol{S}^T & \boldsymbol{R} \end{bmatrix} \tag{74}$$

The fact that $\imath$ needs to go to infinity is explained by the non-stationarity of the Kalman filter in (71) for finite $\imath$ values, see Van Overschee and De Moor (1996).

Choice of weighting matrices. The general formulation of the CSI-data algorithm presented above leaves some freedom in the choice of the weighting matrices $\boldsymbol{W_1}$ and $\boldsymbol{W_2}$. In order not to lose the consistency property, it is obvious that $\boldsymbol{W_1}$ should be of full rank, and that $\boldsymbol{W_2}$ should preserve the rank of the matrices with which it is multiplied. It was shown by Van Overschee and De Moor (1994b) that by specific choices of the weighting matrices, the N4SID algorithm of Van Overschee and De Moor (1994a), the PO-MOESP algorithm of Verhaegen (1994), and the CVA algorithm of Larimore (1990) can be obtained. However, it is well known that an oblique projection, which is an essential step in the algorithm (49), is a numerically ill-conditioned problem. Goethals (2005) indicated that the ill-conditioning can be removed by choosing $\boldsymbol{W_1}$ and $\boldsymbol{W_2}$ in such a way that $\boldsymbol{W_1 \mathcal{O}_i W_2}$ consists of an orthogonal projection. A possible choice is $\boldsymbol{W_1} = \boldsymbol{I}$ and $\boldsymbol{W_2} = \boldsymbol{P}^{\perp}_{\mathscr{U}_{i|2i-1}}$, with $\boldsymbol{P}^{\perp}_{\mathscr{U}_{i|2i-1}}$ the orthogonal projector onto the orthogonal complement of $\mathscr{U}_{i|2i-1}$. This corresponds to the PO-MOESP algorithm. Also for CSI-data/ref, the rule of thumb (65) for the choice of i is advised.

Implementation. The CSI-data/ref algorithm can, like the SSI-data/ref algorithm, be efficiently implemented by making use of the LQ-factorisation technique, where the explicit computation of the Q factor can be avoided. The interested reader is referred to (Reynders and De Roeck, 2008) for the implementation details.

5 Estimation of the modal parameters

5.1 Introduction

When a state-space model is identified from measured input-output or output-only data, a free vibration analysis and a modal decomposition of the identified model results in eigenfrequencies, damping ratios, mode shapes, and modal participation vectors of the structure. If a driving point measurement is made, absolute mode scaling is possible as well.

5.2 Estimation of the modal parameters

When a discrete-time deterministic $(\boldsymbol{A}, \boldsymbol{B}, \boldsymbol{C}, \boldsymbol{D})$ or stochastic state-space model $(\boldsymbol{A}, \boldsymbol{G^{(ref)}}, \boldsymbol{C}, \boldsymbol{\Lambda_0}/2)$ is identified, the modal parameters can be estimated as follows. The eigenvalue decomposition (14) leads to the system description in modal form (15-16), from which the unscaled mode shapes $\boldsymbol{\phi_j}$ and the discrete-time modal participation vectors $\boldsymbol{l_{dj}}$ are imme-

diately obtained. From the ZOH map (11), it follows that

$$\lambda_{cj} = \frac{\ln(\lambda_{dj})}{T}. \tag{75}$$

The undamped frequency and damping ratio are then obtained as

$$f_{uj} = \frac{|\lambda_{cj}|}{2\pi} \qquad \text{and} \qquad \xi_j = \frac{-\lambda_{cjR}}{|\lambda_{cj}|}, \tag{76}$$

respectively. Reynders and De Roeck (2008) showed that, when at least one driving point measurement is made, and the response DOFs are displacements, velocities, or accelerations, the modal scaling factors can be obtained from the following expression:

$$q_j = \text{vec}\left(\frac{i\omega - \lambda_{cj}}{e^{i\omega T} - \lambda_{dj}} \begin{bmatrix} \boldsymbol{\phi_{jv}} \\ i\omega\boldsymbol{\phi_{j\dot{v}}} \\ \omega^2\boldsymbol{\phi_{j\ddot{v}}} \end{bmatrix} \boldsymbol{\phi_{je}^T}\right)^{\dagger} \text{vec}\left(\begin{bmatrix} \boldsymbol{\phi_{jv}} \\ \boldsymbol{\phi_{j\dot{v}}} \\ \frac{1-e^{i\omega T}}{\lambda_{dj}-1}\boldsymbol{\phi_{j\ddot{v}}} \end{bmatrix} \boldsymbol{l_{dj}^T}\right), \tag{77}$$

where the subscripts $\square_v$, $\square_{\dot{v}}$, and $\square_{\ddot{v}}$ select the displacement, velocity, and acceleration response DOFs, respectively. Since in an identified model, it is most probable that the contribution of a mode is modeled best near its resonance frequency, it is suggested to choose $\omega = \omega_j$ for the estimation. Alternatively, a series of frequencies, containing for example also the half power points, could be used. For the scaling of the mode shapes, two schemes are quite popular.

- In the *unit modal displacement* weighting scheme, the mode shape $\boldsymbol{\phi_j}$ is scaled in such a way that one of the elements, usually the one with the largest amplitude, of the scaled mode shape $\boldsymbol{\varphi_j}$ is unity:

$$\boldsymbol{\varphi_j} = \frac{\boldsymbol{\phi_j}}{\phi_{j,k}}. \tag{78}$$

- When a driving point FRF can be calculated, the *unity modal mass* weighting scheme leads to (Heylen et al., 1997)

$$\boldsymbol{\varphi_j} = \sqrt{2\lambda_{cj}q_j}\boldsymbol{\phi_j}. \tag{79}$$

5.3 Distribution of the estimates

In Section 4.2, the distributions of the parameters estimated with SSI-cov/ref were found to be asymptotically normally distributed because of the central limit theorem and the fact that a linear combination of normally distributed random variables is again normally distributed. Since the

coefficient of variation of the estimated parameters is usually low, a linear sensitivity analysis of the modal parameters as a function of the model parameters is sufficiently accurate to determine the covariances of the modal parameters. Their distribution is then asymptotically normal.

Discrete-time and continuous-time poles. As shown by Reynders et al. (2008), one has that, for the discrete-time poles λ_{dj},

$$\Delta\lambda_{dj,re} \approx \underbrace{\left(\frac{(\boldsymbol{\psi_{dj}} \otimes \overline{\boldsymbol{\chi_{dj}}})^T}{\boldsymbol{\chi}_{\boldsymbol{dj}}^* \boldsymbol{\psi_{dj}}} \right)_{re}}_{\triangleq \boldsymbol{J}_{\boldsymbol{\lambda_{dj}}}} \mathrm{vec}(\Delta \boldsymbol{A}),$$

where $\boldsymbol{\chi_{dj}}$ and $\boldsymbol{\psi_{dj}}$ denote the left and right eigenvectors corresponding to the eigenvalue λ_{dj} of $\boldsymbol{A}$, respectively.

The relationship between the discrete-time system poles and the continuous-time system poles is given by (75). It follows that the real and imaginary parts of λ_{cj} are given as

$$\lambda_{cjR} = \frac{\ln|\lambda_{dj}|^2}{2T} \qquad \text{and} \qquad \lambda_{cjI} = \frac{1}{T}\tan^{-1}\left(\frac{\lambda_{djI}}{\lambda_{djR}}\right). \tag{80}$$

A linear sensitivity analysis of these expressions leads to (Pintelon et al., 2007)

$$\Delta\boldsymbol{\lambda_{cj,re}} = \boldsymbol{J}_{\boldsymbol{\lambda_{cj}}} \Delta\boldsymbol{\lambda_{dj,re}}, \qquad \text{where} \qquad \boldsymbol{J}_{\boldsymbol{\lambda_{cj}}} \triangleq \frac{1}{T|\lambda_{dj}|^2} \begin{bmatrix} \lambda_{djR} & \lambda_{djI} \\ -\lambda_{djI} & \lambda_{djR} \end{bmatrix}.$$

Eigenfrequencies and damping ratios. The relationship between the eigenfrequencies, damping ratios and the continuous-time system poles is given by (76). A linear sensitivity analysis of these expressions yields (Pintelon et al., 2007)

$$\begin{bmatrix} \Delta f_j \\ \Delta\xi_j \end{bmatrix} = \boldsymbol{J}_{\boldsymbol{f_j\xi_j}} \Delta\boldsymbol{\lambda_{cj,re}}, \quad \text{where} \quad \boldsymbol{J}_{\boldsymbol{f_j\xi_j}} \triangleq \frac{1}{|\lambda_{cj}|} \left[\begin{array}{c|c} \frac{\lambda_{cjR}}{2\pi} & \frac{\lambda_{cjI}}{2\pi} \\ \hline -\frac{\lambda_{cjI}{}^2}{|\lambda_{cj}|^2} & \frac{\lambda_{cjR}\lambda_{cjI}}{|\lambda_{cj}|^2} \end{array}\right].$$

Mode shapes. In order to derive the first-order sensitivity of the mode shapes, the first-order sensitivity of the eigenvectors $\boldsymbol{\psi_{dj}}$ of $\boldsymbol{A}$ is needed. For the generic case, where $\boldsymbol{A}$ has n different eigenvalues, a first-order perturbation of $\boldsymbol{\psi_{dj}}$ with respect to the elements of $\boldsymbol{A}$ was derived by Reynders

et al. (2008):

$$\Delta\boldsymbol{\psi_{dj}} \approx \underbrace{\left(\boldsymbol{I} - \frac{\boldsymbol{A}}{\lambda_{dj}}\right)^{\dagger} \frac{1}{\lambda_{dj}} \left(\boldsymbol{\psi_{dj}^{T}} \otimes \left(\boldsymbol{I} - \frac{\boldsymbol{\psi_{dj}}\boldsymbol{\chi_{dj}^{*}}}{\boldsymbol{\chi_{dj}^{*}}\boldsymbol{\psi_{dj}}}\right)\right)}_{\triangleq \boldsymbol{J_{\psi_{dj}}}} \mathrm{vec}(\boldsymbol{\Delta A}). \tag{81}$$

Using Kronecker algebra, the first-order perturbation of the corresponding mode shape $\boldsymbol{\phi_j}$ can be calculated:

$$\Delta\boldsymbol{\phi_{j,re}} \approx (\boldsymbol{C}\Delta\boldsymbol{\psi_{dj}} + \Delta\boldsymbol{C}\boldsymbol{\psi_{dj}})_{re} = \left[\begin{array}{c|c} \boldsymbol{J_{\psi_{dj}}} & \boldsymbol{\psi_{dj}^{T}} \otimes \boldsymbol{I_{n_y}} \end{array}\right]_{re} \begin{bmatrix} \mathrm{vec}(\Delta\boldsymbol{A}) \\ \mathrm{vec}(\Delta\boldsymbol{C}) \end{bmatrix}.$$

When the modes are scaled to a unit modal displacement in one of the degrees of freedom, a first-order sensitivity analysis of (78) leads to

$$\Delta\boldsymbol{\varphi_{j,re}} \approx \underbrace{\left(\frac{1}{\phi_{j,k}}\left(\boldsymbol{I} - \boldsymbol{\varphi_j}\boldsymbol{S_{\phi_{j,k}}}\right)\right)_{Re}}_{\boldsymbol{J_{\varphi_j}}} \Delta\boldsymbol{\phi_{j,re}},$$

where $\boldsymbol{S_{\phi_{j,k}}} \triangleq \begin{bmatrix}\boldsymbol{0_{1,k-1}} & 1 & \boldsymbol{0_{1,n_y-k}}\end{bmatrix}$.

Covariance matrix of the modal parameters. Combining the sensitivity formulae for the modal parameters derived above, their complete covariance matrix is obtained:

$$\mathrm{Cov}\left(\begin{bmatrix} f_j \\ \xi_j \\ \boldsymbol{\varphi_{j,re}} \end{bmatrix}, \begin{bmatrix} f_l \\ \xi_l \\ \boldsymbol{\varphi_{l,re}} \end{bmatrix}\right) = \boldsymbol{J_{f\xi\varphi,j}} \mathrm{cov}\left(\begin{bmatrix} \mathrm{vec}(\hat{\boldsymbol{A}}) \\ \mathrm{vec}(\hat{\boldsymbol{C}}) \end{bmatrix}\right) \boldsymbol{J_{f\xi\varphi,l}^{T}}, \tag{82}$$

where

$$\boldsymbol{J_{f\xi\varphi,j}} \triangleq \begin{bmatrix} \boldsymbol{J_{f_j\xi_j}}\boldsymbol{J_{\lambda_{cj}}}\boldsymbol{J_{\lambda_{dj}}} & \boldsymbol{0_{2\times n_y n}} \\ \boldsymbol{J_{\psi_{dj}}}\boldsymbol{J_{\varphi_j}} & \left(\boldsymbol{\psi_{dj}^{T}} \otimes \boldsymbol{I_{n_y}}\right)\boldsymbol{J_{\varphi_j}} \end{bmatrix}.$$

Distribution of damping ratios for lightly damped modes. When a mode is lightly damped, it follows from (80) that the real part of its continuous-time pole, λ_{cjR}, is not only close to zero, but it also has a potentially large coefficient of variation, such that a linear sensitivity analysis, as presented above, is not sufficiently accurate for determining its asymptotic *Probability Density Function* (PDF). This affects significantly the PDF of the damping ratio, see (76), but not of the other modal parameters. Since the damping ratio ξ_j is a nonlinear function of the discrete-time system

pole λ_{dj} only, and since the real and imaginary parts of λ_{dj} are to a good approximation asymptotically jointly normally distributed, the PDF of ξ_j can be calculated using a Monte Carlo simulation, where the joint PDF of $\lambda_{dj,re}$, estimated using the linear sensitivity approach, is sampled. Because each Monte Carlo simulation step is computationally very cheap, the total computational cost of this approach is sufficiently low for modal testing.

6 Applications

6.1 Introduction.

In this section, the application of operational modal analysis techniques, with and without exogenous forces, is investigated for two different types of structures.

In Section 6.2, the feasibility of using an exogenous force in operational modal testing of a prestressed concrete bridge is investigated. The performance of the CSI-data/ref algorithm on the shaker data of the Z24 bridge, that have been proposed as a benchmark for testing modal parameter estimation algorithms, is investigated and compared with previously reported results.

The second application deals with operational modal analysis of a steel transmitter mast under wind loading, and is presented in Section 6.3. The goal is to demonstrate the feasibility of estimating confidence intervals on modal parameters obtained from a *single* operational modal test.

6.2 Z24 bridge

Introduction. The Z24 bridge was part of the road connection between the villages of Koppigen and Utzenstorf, Switzerland, over-passing the A1 highway between Bern and Zürich. It was a classical post-tensioned concrete two-cell box-girder bridge with a main span of 30m and two side spans of 14m, see Figure 8. The bridge was built as a free standing frame with the approaches backfilled later. Both abutments consisted of triple concrete columns connected with concrete hinges to the girder. Both intermediate supports were concrete piers clamped into the girder. An extension of the bridge girder at the approaches provided a sliding slab. All supports were rotated with respect to the longitudinal axis which yielded a skew bridge. The bridge, that dated from 1963, was demolished at the end of 1998, because a new railway adjacent to the highway required a new bridge with a larger side span.

Before complete demolition, the bridge was subjected to a long-term continuous monitoring test and a short-term progressive damage test in the

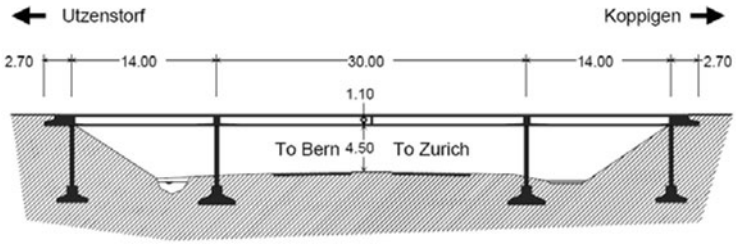

Figure 8. Side view of the Z24 bridge. Distances are in m.

framework of the Brite-EuRam project CT96 0277 SIMCES (De Roeck, 2003).

- A *long-term continuous monitoring test* took place during the year before demolition. The aim was to quantify the environmental variability of the bridge dynamics.
- A *Progressive Damage Test* (PDT) took place in a one-month time period, shortly before complete demolition. The aim was to prove experimentally that realistic damage has a measurable influence on bridge dynamics. Each PDT step alternated with short-term modal tests, while the continuous monitoring system was still running during these tests.

In order for the applied damage scenarios to be significant and realistic, it was made sure that (1) they were relevant for the safety of the bridge and (2) the simulated damage occurred frequently, a condition which was checked in the literature and by questioning Swiss bridge owners. Since the A1 highway was never closed to traffic, some damage scenarios that meet these criteria could not be applied without reducing the safety of the traffic which was considered of paramount importance. The traffic on the Z24 bridge was diverted to the A36 highway. Table 1 gives a complete overview of all progressive damage tests that were performed.

Before and after each applied damage scenario, the bridge was subjected to a forced and an ambient vibration test. Since the ambient forces such as wind excitation or traffic under the bridge could not be excluded during the vibration measurements, all modal tests can be considered as operational tests, with or without the use of artificial (exogenous) forces. With a measurement grid consisting of a regular 3×45 grid on top of the bridge deck and a 2×8 grid on each of the two pillars, 291 degrees of freedom were measured: all three displacement components on the pillars, and mainly vertical and lateral displacements on the bridge deck. Because of the limited num-

No.	Date (1998)	Scenario	Description / Simulation of real damage cause
1	04.08	1^{st} reference measurement	Healthy structure
2	09.08	2^{nd} reference measurement	After installation of lowering system
3	10.08	Lowering of pier, 20 mm	Settlement of subsoil, erosion
4	12.08	Lowering of pier, 40 mm	
5	17.08	Lowering of pier, 80 mm	
6	18.08	Lowering of pier, 95 mm	
7	19.08	Tilt of foundation	Settlement of subsoil, erosion
8	20.08	3^{rd} reference measurement	After lifting of bridge to initial position
9	25.08	Spalling of concrete, 12 m^2	Vehicle impact, carbonisation and
10	26.08	Spalling of concrete, 24 m^2	subsequent corrosion of reinforcement
11	27.08	Landslide at abutment	Heavy rainfall, erosion
12	31.08	Failure of concrete hinge	Chloride attack, corrosion
13	02.09	Failure of anchor heads I	Corrosion, overstress
14	03.09	Failure of anchor heads II	
15	07.09	Rupture of tendons I	Erroneous or forgotten injection of
16	08.09	Rupture of tendons II	tendon tubes, chloride influence
17	09.09	Rupture of tendons III	

Table 1. Z24 progressive damage test: overview of applied damage scenarios.

ber of accelerometers and acquisition channels, the data were collected in 9 setups using 5 reference channels, see Figure 9. The forced excitation was applied by two vertical shakers of EMPA, Switzerland, placed on the bridge deck. A 1kN shaker was placed on the middle span and a 0.5kN shaker was placed at the Koppigen side span, see figure 8. The shaker input signals were generated with an inverse FFT algorithm, resulting in a fairly flat force spectrum between 3 and 30Hz. After scenario 8, a drop weight test was also performed. The applied shaker and drop weight forces were periodic with 8 periods. In each modal test, a total of 65536 samples were collected at a sampling rate of 100Hz, using an anti-aliasing filter with a 30Hz cut-off frequency. Krämer et al. (1999) provide a detailed description of all vibration tests on the Z24 bridge.

The measurement data have been used for two benchmarks.

- The shaker, ambient and drop weight vibration data from the third reference measurement on the Z24 bridge (scenario 8, Table 1) were presented as a benchmark study for system identification methods for operational modal analysis at the IMAC XIX conference in 2001.
- The data from the long-term continuous monitoring test and the progressive damage test were presented as benchmark data for al-

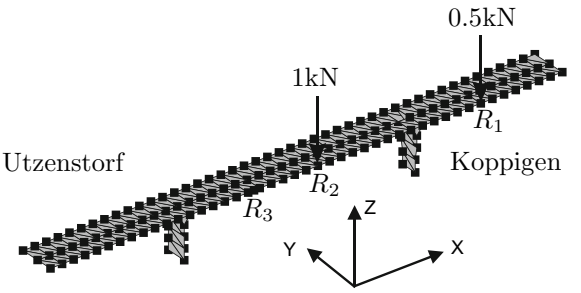

Figure 9. Z24 bridge: Measurement grid, reference positions and shaker positions.

gorithms for structural health monitoring and damage identification in the framework of the European Cost Action F3.

Reynders and De Roeck (2009) provide a literature review of benchmark results. Here, the benchmark shaker data from PDT scenario 8 are used to test the performance of the CSI-data/ref algorithm with respect to the results presented in the literature.

Previous results. Peeters and Ventura (2003) compared the modal parameter estimates obtained by 7 different research teams in the framework of the system identification benchmark with the data from scenario 8. In addition, new modal parameter estimation techniques have been validated on the benchmark data, such as a parametric and nonparametric setup assembly approach followed by maximum likelihood estimation, proposed by Parloo et al. (2003), and an iterative SDOF technique, proposed by Allen and Ginsberg (2006). The best reported result was obtained by applying a subspace identification algorithm (Peeters and Ventura, 2003) and a maximum likelihood algorithm (Parloo et al., 2003) to the shaker data. In this way, 10 modes could be determined.

Results obtained with CSI-data/ref. When analyzing the shaker data of damage scenario 8 for the system identification benchmark, both the classical CSI-data algorithm and the reference-based version CSI-data/ref were used. For CSI-data, $\imath = 30$ was chosen, and a stabilisation diagram of good quality was constructed up to a model order of 160. For CSI-data/ref, the 5 acceleration channels common to every setup were chosen to be the

references for the identification, $\imath = 50$ was chosen, and a stabilisation diagram of good quality was constructed up to a model order of 160. Note that, in order to obtain similar computation time and memory usage, the values of $\imath$ differ for CSI-data and CSI-data/ref. A choice of $\imath = 30$ for both CSI-data and CSI-data/ref would have resulted in a faster calculation and a smaller memory usage for CSI-data/ref. According to the rule of thumb (65), the choice of $\imath$ corresponds to $f_0 = 1.67$Hz for CSI and $f_0 = 1$Hz for CSI/ref.

From the stabilisation diagram constructed with the CSI-data and CSI-data/ref methods, 13 and 14 modes could be identified, respectively. Table 2 shows the sample mean values of the eigenfrequencies and damping ratios, obtained with each method, as well as the sample standard deviations, calculated from the 9 different setups. The CSI-data/ref method clearly yields more accurate estimates of both eigenfrequencies and damping ratios for modes 3, 6 and 8, while the opposite is true for mode 7. With the CSI-data/ref method, one more mode could be obtained than with the CSI-data method. Table 2 also shows the MAC values between the corresponding mode shapes determined using CSI-data and CSI-data/ref. The mode shapes are all very well correlated. An almost perfect correlation is observed for modes 1, 2, 5, 6, 7, 8 and 10. Mode 9 has the lowest MAC value, which indicates that the mode shape estimated with one or both methods is of a lower quality than the other modes. This corresponds to a relatively high uncertainty on the eigenfrequency and damping ratio of mode 9 for both CSI-data and CSI-data/ref.

Figure 10 shows the identified bending modes. Mode 13 could only be identified with CSI-data/ref. The identified lateral modes are plotted in Figure 11. The identification of these modes proves experimentally that the combined deterministic-stochastic subspace identification method enables one to identify modes excited by both forced or ambient loading or a combination of both. Indeed, these lateral modes are almost exclusively excited by ambient forces. Modes 3 and 4 were not detected in previous studies. The quality of the mode shape of mode 4 is lower because the only horizontal reference DOF is located near the center of the middle span, in the zone with almost zero modal displacement. This results in a 'stepped' mode shape.

Due to the skewness of the bridge supports, some modes occur where bending and torsion are combined. Two of these modes are shown in Figure 12. Their eigenfrequencies are closely spaced. Although they look very similar, they are truly different, as is confirmed by their experimental MAC value (Heylen et al., 1997) of 0.18 for CSI-data/ref.

Figure 13 shows the higher torsion modes that were identified. The mode

mode	CSI-data				CSI-data/ref				MAC
	f(Hz)	σ_f(Hz)	ξ(%)	σ_d(%)	f(Hz)	σ_f(Hz)	ξ(%)	σ_d(%)	
1	3.871	0.001	0.89	0.05	3.871	0.002	0.88	0.04	1.00
2	4.823	0.008	1.63	0.06	4.818	0.011	1.66	0.04	1.00
3	6.697	0.127	4.23	1.45	6.722	0.028	3.82	0.62	0.98
4	8.355	0.059	8.91	1.77	8.346	0.104	9.37	1.33	0.96
5	9.769	0.005	1.54	0.03	9.772	0.005	1.57	0.02	1.00
6	10.51	0.011	1.45	0.06	10.50	0.007	1.43	0.04	1.00
7	12.42	0.020	3.11	0.03	12.42	0.025	3.15	0.12	1.00
8	13.21	0.033	4.76	0.29	13.21	0.018	4.72	0.17	1.00
9	17.45	0.212	4.34	0.38	17.52	0.169	3.64	1.39	0.92
10	19.27	0.019	2.43	0.10	19.28	0.022	2.46	0.06	1.00
11	19.68	0.080	5.58	0.31	19.65	0.113	5.51	0.29	0.98
12	26.64	0.054	3.20	0.11	26.62	0.055	3.12	0.11	0.95
13	/	/	/	/	33.18	0.202	4.33	1.78	/
14	37.25	0.198	3.69	0.48	37.20	0.106	3.94	0.61	0.95

Table 2. Z24 bridge, scenario 8: eigenfrequencies f_j and damping ratios ξ_j determined with CSI-data and CSI-data/ref, and MAC values between corresponding mode shapes.

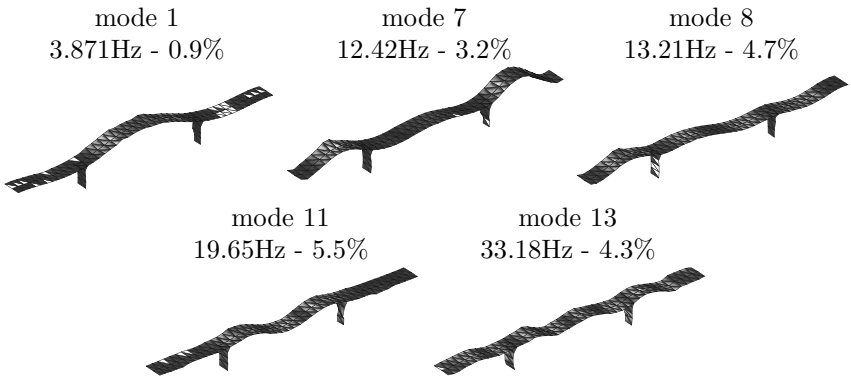

Figure 10. Z24 bridge, scenario 8: bending modes identified with CSI-data(/ref).

shape of mode 9 is less smooth than the mode shapes of the other modes; this corresponds to the higher uncertainty on the corresponding eigenfrequency and damping ratio (Table 2). In mode 12, the Koppigen pier (Figure 9) has the highest participation, which could be due to the fact that a cut

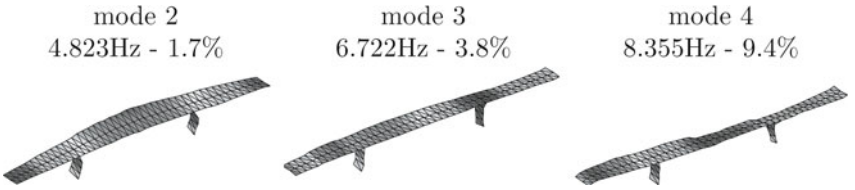

Figure 11. Z24 bridge, scenario 8: lateral modes identified with CSI-data(/ref).

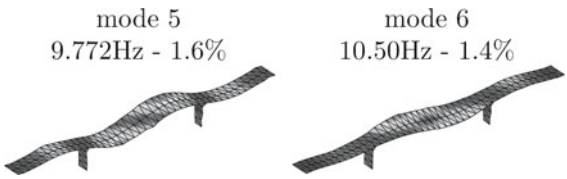

Figure 12. Z24 bridge, scenario 8: two closely spaced mixed torsion/bending modes identified with CSI-data(/ref).

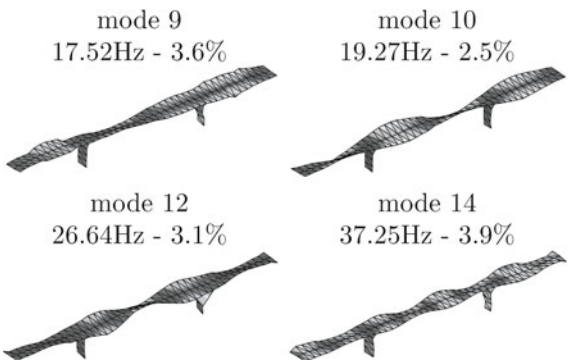

Figure 13. Z24 bridge, scenario 8: higher torsion modes identified with CSI-data(/ref)

was made through this pier for the simulation of a settlement: although the

mode	DOF	CSI		CSI/ref	
		u(mm)	σ_u(mm)	u(mm)	σ_u(mm)
1	R_2z	1.28 + 0.06i	0.05 + 0.04i	1.30 + 0.07i	0.03 + 0.03i
2	R_2y	-1.38 + 0.38i	0.18 + 0.21i	1.38 + 0.15i	0.13 + 0.06i
3	R_2y	-0.22 - 0.22i	0.10 + 0.19i	0.15 + 0.13i	0.09 + 0.30i
4	R_3z	0.27 + 0.05i	0.18 + 0.13i	0.46 + 0.13i	0.20 + 0.16i
5	R_3z	-3.69 - 0.42i	0.42 + 0.14i	3.75 + 0.55i	0.36 + 0.22i
6	R_2z	1.16 + 0.29i	0.05 + 0.07i	-1.11 - 0.25i	0.05 + 0.05i
7	R_1z	-4.74 - 0.83i	0.23 + 0.09i	-4.65 - 0.75i	0.27 + 0.19i
8	R_1z	-3.01 - 0.63i	0.41 + 0.19i	2.96 + 0.70i	0.16 + 0.13i
9	R_1z	-3.11 - 1.35i	0.55 + 0.59i	-2.34 - 1.04i	1.29 + 0.71i
10	R_3z	3.08 + 1.05i	0.33 + 0.19i	3.12 + 1.16i	0.31 + 0.07i
11	R_2z	-0.92 - 0.33i	0.38 + 0.18i	-0.94 - 0.19i	0.23 + 0.18i
12	R_2z	-1.36 - 0.42i	0.08 + 0.11i	1.31 + 0.32i	0.11 + 0.12i
13	R_2z	/	/	-0.39 - 0.07i	0.19 + 0.54i
14	R_1z	1.53 + 1.55i	0.58 + 0.34i	-1.73 - 1.63i	0.47 + 0.39i

Table 3. Z24 bridge, scenario 8: modal displacements, scaled to unity modal mass. The standard deviations consist of the standard deviation of the real part and the standard deviation of the imaginary part of the corresponding displacement. They are the sample standard deviations for the total of nine setups.

settlement was removed, the original state was only approximately reached. The identification of mode 14 at 37.25Hz, despite the fact that the cut-off frequency of the analog anti-aliasing filter was set to 30Hz, indicates that the method is able to identify modes that are only very weakly present in the data.

Modes 1, 2, 5, 6, 7, 8, 9, 10, 11 and 12 have been detected in previous benchmark analyses; the other modes were only detected in the present study. Because CSI-data and CSI-data/ref identify a combined deterministic-stochastic state-space model, they enable a mass-normalisation of the modes that are excited by the deterministic forces. Table 3 shows, for each scaled mode, the largest of the reference displacement DOFs (Figure 9). From this table, bearing in mind that none of the identified modes is truly complex, the following can be noticed.

- For modes 1, 5, 6, 7, 8, 10, 11 and 12, all in the frequency band of forced excitation (3-30Hz), the largest reference displacements are in the direction of the forced excitation and the real part of the scaled

mode shapes is much larger than the imaginary part. This indicates that they are properly scaled.
- Although mode 2 is mainly a lateral mode and the forced excitation is purely vertical, the real part of the scaled mode shape is much larger than the imaginary part. Together with the small sample variance of the modal displacement, this is an indication that the mode is properly scaled.
- As indicated by the large imaginary part and the large sample variance, the lateral modes 3 and 4 are not properly scaled because they are not well excited by the artificial forces. However, using an OMAX approach, it is possible to identify these modes because they are excited by ambient forces.
- The rather large uncertainty on the scaled displacements of mode 9 corresponds to the large uncertainty on the frequency and damping ratio (Table 2) and the quality of the mode shape (Figure 13).
- Modes 13 and 14 can not be properly scaled, as their eigenfrequencies lie outside the frequency band of the forced excitation and above the cut-off frequency of the anti-aliasing filter.

6.3 Steel transmitter mast

Introduction. In this section, the SSI-cov/ref algorithm is applied to the operational modal analysis of a truss structure, situated in the harbor of Antwerp, Belgium. It is a mast of 30m height which contains sectorial antennae for a cellular phone network at the top (Figure 14). The antennae comprise about 10% of the total weight of the structure.

Vibration measurements and signal preprocessing. On March 26, 1998, an ambient vibration test was performed on the structure. Peeters and De Roeck (1999) presented the results of this test. Here, their uncertainty is investigated.

The aim of the test was to investigate the structure's modal parameters, particularly the damping ratios, in the frequency range of $0 - 5$Hz. 17 degrees of freedom (DOFs), all horizontal accelerations, have been measured in 3 setups using 3 reference DOFs that were common to each setup. Three horizontal accelerations were measured at heights of 6.17m, 12.17m, 18.17m, 24.17m and 29.90m. If it is assumed that the cross-section of the mast remains undeformed during the vibration test, which is a reasonable assumption in the frequency band considered, three DOFs are sufficient to describe the complete horizontal movement of the cross-section. Two orthogonal accelerations at the top of the mast (at a height of 33.00m) were measured as well.

Figure 14. Steel mast with sectorial antennae at the top.

The data were sampled at a rate of 100Hz. The cut-off frequency of the anti-aliasing filter was set to 20Hz. The number of samples was set to $N = 30720$, which resulted in a measurement time of approximately 5 minutes. Afterwards, the data were digitally filtered with a low-pass filter with a cut-off frequency of 5Hz and re-sampled at 12.5Hz, which reduced the number of samples to $N = 3840$.

Modal parameters. With SSI-cov/rev, the eigenfrequencies, damping ratios, and mode shapes, as well as covariances of these modal parameters, are identified for each individual setup. The identification parameters are $\imath = 10$, $n = 20$ and $n_b = 100$. According to the rule of thumb (65), the choice of $\imath$ corresponds to $f_0 = 0.63$Hz. The parts of the mode shapes that result from the different setups are combined with linear least squares. They are scaled to 1 in one of the reference DOFs. The variances of the different modal displacements are adopted accordingly.

The identified eigenfrequencies and their estimated 95% confidence intervals are shown in Table 4. The eigenfrequency estimates obtained in each setup match very well. The estimated confidence intervals correspond very well with the variation of the actual values from setup to setup.

The identified damping ratios and their estimated 95% confidence intervals are shown in Table 5. The damping ratio estimates differ quite a lot from setup to setup, which is also reflected in the high values of the

mode	setup 1	setup 2	setup 3
1	1.172 ± 0.003	1.168 ± 0.006	1.166 ± 0.004
2	1.178 ± 0.005	1.178 ± 0.005	1.180 ± 0.005
3	1.948 ± 0.009	1.956 ± 0.008	1.951 ± 0.004
4	2.603 ± 0.006	2.599 ± 0.008	2.601 ± 0.006
5	2.711 ± 0.002	2.712 ± 0.007	2.711 ± 0.004
6	3.686 ± 0.008	3.689 ± 0.005	3.685 ± 0.006
7	4.632 ± 0.010	4.633 ± 0.011	4.631 ± 0.008

Table 4. Steel mast: identified eigenfrequencies (in Hz) with their estimated 95% confidence interval.

estimated confidence intervals. Because of their high relative uncertainty, the confidence intervals of the damping ratios are calculated using a Monte Carlo sampling of the discrete-time poles, which have a low relative uncertainty. The values obtained from a linear sensitivity approach are given between brackets. Despite the large relative uncertainty on the damping ratios, both estimates for the confidence intervals agree very well.

The identified mode shapes and their estimated 95% confidence interval are shown in Figure 15. Only the third mode is a torsion mode, the other modes are bending modes. It can be seen that the mode shapes of modes 3 through 6 are very accurate, mode 7 is fairly accurate and modes 1 and 2 are inaccurate. This difference in mode shape quality is also apparent when the real and imaginary parts of the identified modes are plotted in the complex plane (see Figure 16): while modes 3 through 7 are fairly real, modes 1 and 2 have important imaginary components.

This can be physically understood from the fact that the structure is almost triply symmetric, since perfect multiple symmetric structures have pairs of eigenmodes with identical eigenfrequencies, reflecting that the mode shapes are indefinite. Dooms et al. (2006) illustrate this for a nearly axisymmetric structure. Here, the symmetry is somewhat disturbed by the diagonals and a ladder at one of the masts. Only the first two modes are very close, with estimated eigenfrequencies of 1.172 and 1.178Hz in the first setup. The next pair of bending modes are already better separated, thanks to the symmetry disruptions, with eigenfrequencies at 2.602 and 2.711Hz.

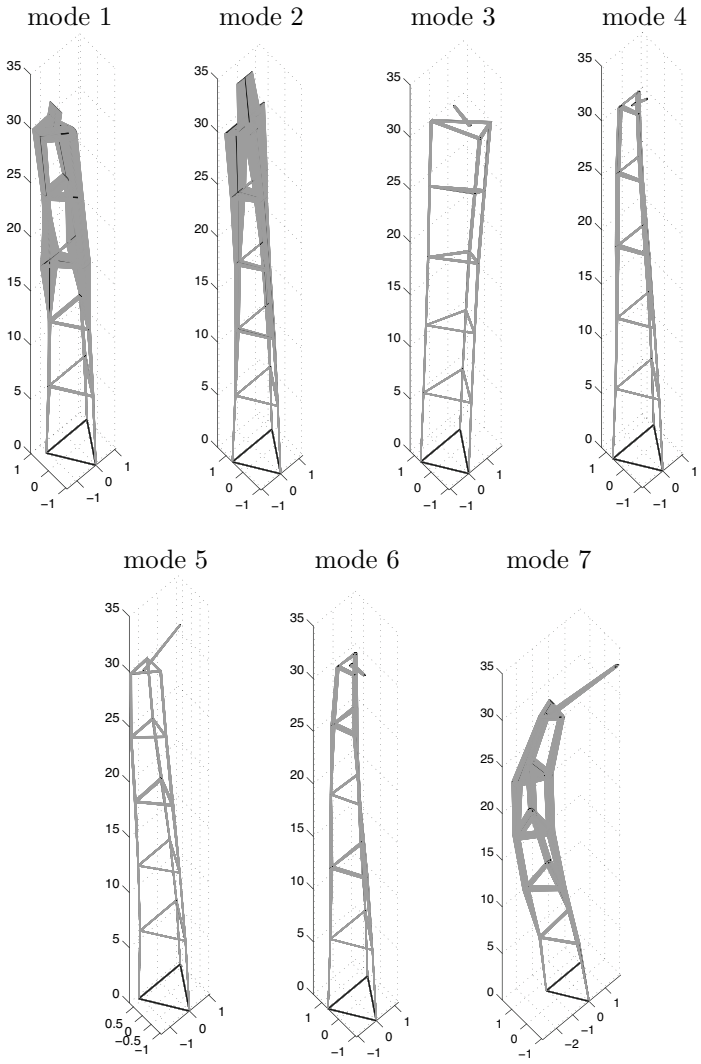

Figure 15. Steel mast: identified mode shapes (black) with their estimated 95% confidence interval (grey).

mode	setup 1	setup 2	setup 3
1	0.14 ± 0.26 (0.26)	0.55 ± 0.42 (0.42)	0.60 ± 0.35 (0.37)
2	0.67 ± 0.33 (0.37)	0.57 ± 0.42 (0.43)	0.95 ± 0.45 (0.45)
3	0.64 ± 0.32 (0.31)	0.80 ± 0.27 (0.26)	0.47 ± 0.22 (0.22)
4	0.36 ± 0.26 (0.28)	0.57 ± 0.39 (0.39)	0.35 ± 0.21 (0.21)
5	0.08 ± 0.09 (0.10)	0.27 ± 0.19 (0.22)	0.19 ± 0.11 (0.12)
6	0.28 ± 0.32 (0.33)	0.17 ± 0.18 (0.19)	0.27 ± 0.19 (0.20)
7	0.27 ± 0.23 (0.23)	0.16 ± 0.46 (0.51)	0.18 ± 0.15 (0.17)

Table 5. Steel mast: identified damping ratios (in %) with their estimated 95% confidence interval, estimated from a Monte Carlo sampling of the discrete-times poles and using a linear sensitivity analysis (between brackets).

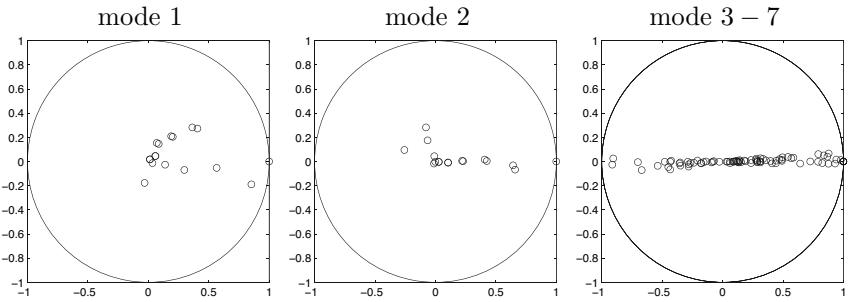

Figure 16. Steel mast: real vs. imaginary part of the identified modal displacements, scaled to 1 at the largest displacement value.

7 Conclusions

This chapter addressed the extraction of eigenfrequencies, damping ratios, mode shapes and, whenever possible, modal scaling factors, from measured operational data.

A conversion between finite element models, that are frequently used in forward modeling of vibrating structures, and discrete-time state-space models, that are identified from measured data, was derived. This confirms that the latter models are valid also from a forward point of view. Furthermore, it was shown that modeling the operational excitation due to turbulent fluid pressure, micro-tremors, or roadway or footfall excitation,

as stochastic quantities, has a clear physical basis. This justifies the use of stochastic system identification algorithms for OMA, and the use of combined deterministic-stochastic system identification algorithms for OMAX.

The use of subspace identification methods and their predecessors, system realisation methods, for the identification of stochastic and combined deterministic-stochastic state-space models from operational data, was discussed. The general ideas that lie behind this class of system identification methods were separated from the algorithms themselves. Two subspace algorithms that are commonly used for OMA were discussed in detail: SSI-cov/ref and SSI-data/ref. For SSI-cov/ref, the probability density function of the identified state-space matrices was derived. Recently, it was shown that the SSI-data/ref is statistically asymptotically efficient, i.e., no estimator with lower asymptotic covariance can be found. This confirms previous experience with subspace identification algorithms, that have shown to outperform alternative system identification algorithms in several comparative studies, see, e.g., Peeters and De Roeck (2001). Since OMAX testing can enhance the current ambient vibration testing practice in the sense that it allows the mode shapes to be mass-normalised and the frequency content of the excitation to be extended, a recently developed subspace algorithm that can be used for OMAX, was presented: CSI-data/ref.

In a first real-life application, this CSI-data/ref algorithm was seen to yield the most complete set of modal parameters for the Z24 bridge benchmark data reported so far. In a second real-life application, the estimation of confidence intervals of modal parameters identified with SSI-cov/ref was illustrated for a steel transmitter mast.

Bibliography

H. Akaike. Stochastic theory of minimal realization. *IEEE Transactions on Automatic Control*, 19(6):667–674, 1974.

H. Akaike. Markovian representation of stochastic processes by canonical variables. *SIAM journal on control*, 13(1):162–173, 1975.

M.S. Allen and J.H. Ginsberg. A global, single-input-multiple-output (SIMO) implementation of the algorithm of mode isolation and application to analytical and experimental data. *Mechanical Systems and Signal Processing*, 20(5):1090–1111, 2006.

B.D.O. Anderson and J.B. Moore. *Optimal filtering*. Prentice Hall, Englewood Cliffs, NJ, 1979.

K.S. Arun and S.Y. Kung. Balanced approximation of stochastic systems. *SIAM journal on matrix analysis and applications*, 11:42–68, 1990.

D. Bauer. Comparing the CCA subspace method to pseudo maximum likelihood methods in the case of no exogenous inputs. *Journal of Time Series Analysis*, 26(5):631–668, 2005.

D. Bauer and L. Ljung. Some facts about the choice of the weighting matrices in Larimore type of subspace algorithms. *Automatica*, 38(5):763–773, 2002.

D. Bauer, M. Deistler, and W. Scherrer. On the impact of weighting matrices in subspace algorithms. In *Proceedings of the 12th IFAC symposium on system identification SYSID 2000*, Santa Barbara, CA, June 2000.

A. Ben-Israel and T. Greville. *Generalized inverses*. John Wiley, New York, NY, 1974.

H. Braun and T. Hellenbroich. Messergebnisse von Strassenunebenheiten. *VDI Berichte*, 877:47–80, 1991.

J.W. Brewer. Kronecker products and matrix calculus in system theory. *IEEE Transactions on Circuits and Systems*, 25(9):772–781, 1978.

B. Cauberghe. *Applied frequency-domain system identification in the field of experimental and operational modal analysis*. PhD thesis, Vrije Universiteit Brussel, 2004.

A. Chiuso and G. Picci. The asymptotic variance of subspace estimates. *Journal of Econometrics*, 118(1–2):257–291, 2004.

R.W. Clough and J. Penzien. *Dynamics of structures*. McGraw-Hill, New York, third edition, 1995.

G. De Roeck. The state-of-the-art of damage detection by vibration monitoring: the SIMCES experience. *Journal of Structural Control*, 10:127–143, 2003.

D. Dooms, G. Degrande, G. De Roeck, and E. Reynders. Finite element modelling of a silo based on experimental modal analysis. *Engineering Structures*, 28(4):532–542, 2006.

E.R. Dougherty. *Random processes for image and signal processing*. SPIE Press, Bellingham, WA, 1999.

P.A. Durbin and G. Medic. *Fluid dynamics with a computational perspective*. Cambridge University Press, New York, NY, 2007.

P.A. Durbin and B.A. Petterson Reif. *Statistical theory and modeling for turbulent flows*. John Wiley & Sons, New York, NY, 2001.

G.F. Franklin, J.D. Powell, and M. Workman. *Digital control of dynamic systems*. Addison-Wesley, Menlo Park, CA, 1998.

I. Goethals. *Subspace identification for linear, Hammerstein and Hammerstein-Wiener systems*. PhD thesis, Katholieke Universiteit Leuven, 2005.

W. Heylen, S. Lammens, and P. Sas. *Modal analysis theory and testing*. Department of Mechanical Engineering, Katholieke Universiteit Leuven, Leuven, Belgium, 1997.

B. Ho and R. Kalman. Effective recontruction of linear state-variable models from input/output functions. *Regelungstechnik*, 14(12):545–548, 1966.

J.-N. Juang. *Applied system identification.* Prentice-Hall, Englewood Cliffs, NJ, 1994.

J.-N. Juang and R.S. Pappa. An eigensystem realization algorithm for modal parameter identification and model reduction. *Journal of Guidance, Control and Dynamics*, 8(5):620–627, 1985.

J.-N. Juang, J.E. Cooper, and J.R. Wright. An eigensystem realization algorithm using data correlations (ERA/DC) for modal parameter identification. *Control-theory and advanced technology*, 4(1):5–14, 1988.

R. Kalman. A new approach to linear filtering and prediction problems. *Journal of Basic Engineering, Transactions of the ASME*, 82D:35–45, 1960.

R. Kalman. Mathematical description of linear dynamical systems. *SIAM journal on control*, 1(2):152–192, 1963.

C. Krämer, C.A.M. de Smet, and G. De Roeck. Z24 bridge damage detection tests. In *Proceedings of IMAC 17, the International Modal Analysis Conference*, pages 1023–1029, Kissimmee, FL, USA, February 1999.

S.Y. Kung. A new identification and model reduction algorithm via singular value decomposition. In *Proceedings of the 12th Asilomar conference on circuits, systems and computers*, pages 705–714, Pacific Grove, CA, 1978.

W.E. Larimore. Canonical variate analysis in identification, filtering and adaptive control. In *Proceedings of the 29th conference on decision and control*, pages 596–604, Honolulu, HI, December 1990.

L. Ljung. *System identification: theory for the user.* Prentice Hall, Upper Saddle River, NJ, second edition, 1999.

H. Nyquist. Thermal agitation of electric charge in conductors. *Physical Review*, 32:110–113, 1928.

ORE. Question C116: Wechselwirkung zwischen Fahrzeugen und gleis, Bericht Nr. 1: Spektrale Dichte der Unregelmässigkeiten in der Gleislage. Technical report, Office for Research and Experiments of the International Union of Railways, Utrecht, NL, 1971.

E. Parloo, P. Guillaume, and B. Cauberghe. Maximum likelihood identification of non-stationary operational data. *Journal of Sound and Vibration*, 268(5):971–991, 2003.

B. Peeters and G. De Roeck. Stochastic system identification for operational modal analysis: A review. *ASME Journal of Dynamic Systems, Measurement, and Control*, 123(4):659–667, 2001.

B. Peeters and G. De Roeck. Reference-based stochastic subspace identification for output-only modal analysis. *Mechanical Systems and Signal Processing*, 13(6):855–878, 1999.

B. Peeters and C. Ventura. Comparative study of modal analysis techniques for bridge dynamic characteristics. *Mechanical Systems and Signal Processing*, 17(5):965–988, 2003.

R. Pintelon, J. Schoukens, and P. Guillaume. Box-Jenkins identification revisited - part III: Multivariable systems. *Automatica*, 43(5):868–875, 2006.

R. Pintelon, P. Guillaume, and J. Schoukens. Uncertainty calculation in (operational) modal analysis. *Mechanical Systems and Signal Processing*, 21(6):2359–2373, 2007.

R. Pintelon, B. Peeters, and P. Guillaume. Continuous-time operational modal analysis in the presence of harmonic disturbances. *Mechanical Systems and Signal Processing*, 22(5):1017–1035, 2008.

E. Reynders and G. De Roeck. Reference-based combined deterministic-stochastic subspace identification for experimental and operational modal analysis. *Mechanical Systems and Signal Processing*, 22(3):617–637, 2008.

E. Reynders and G. De Roeck. Continuous vibration monitoring and progressive damage testing on the Z24 bridge. In C. Boller, F.K. Chang, and Y. Fujino, editors, *Encyclopedia of Structural Health Monitoring*, pages 2149–2158. John Wiley & Sons, 2009.

E. Reynders, R. Pintelon, and G. De Roeck. Uncertainty bounds on modal parameters obtained from Stochastic Subspace Identification. *Mechanical Systems and Signal Processing*, 22(4):948–969, 2008.

P. Van Overschee and B. De Moor. *Subspace identification for linear systems*. Kluwer Academic Publishers, Dordrecht, The Netherlands, 1996.

P. Van Overschee and B. De Moor. N4SID: Subspace algorithms for the identification of combined deterministic-stochastic systems. *Automatica*, 30(1):75–93, 1994a.

P. Van Overschee and B. De Moor. A unifying theorem for three subspace system identification algorithms. In *American Control Conference*, pages 1645–1649, Baltimore, MD, June–July 1994b.

M. Verhaegen. Identification of the deterministic part of MIMO state space models given in innovations from input-output data. *Automatica*, 30(1): 61–74, 1994.

H.P. Zeiger and A.J. McEwen. Approximate linear realizations of given dimension via Ho's algorithm. *IEEE Transactions on Automatic Control*, 19:153, 1974.